NOVEL CARBON NANOFORMS FROM DISCOTIC LIQUID CRYSTALS

[1] *Kengqing Jian,* [1]*Christopher Chan,* [1]*Matthew Sousa,* [1] *Yuming Gao,* [2] *Nancy Yang,* [3]*Michael Paukshto,* [1]*Gregory Crawford,* [1] *Robert Hurt*

[1] Brown University, Providence, RI
[2] Sandia National Laboratories, Livermore CA
[3] Optiva, Inc., South San Francisco

Introduction

Much of the excitement surrounding new carbon nanomaterials can be traced to their *directional* properties, which arise through precise orientation of the graphene layers [1-3]. A long term goal in nanocarbon synthesis is to develop techniques for systematic control of graphene layer arrangement in order to produce nanomaterials with crystal structures tailored for specific applications. A new and general method has been developed for achieving molecular control in carbon materials based on non-covalent assembly of polyaromatics [4-7]. Some polyaromatic liquids form liquid crystalline phases that adopt defined molecular order modes near surfaces (surface anchoring states [5] and in confined nanospaces [6]. Discotic liquid crystals were employed in combination with various inorganic templates to produce "orthogonal-symmetry" nanofibers [6] (see Fig. 1) and nanoporous carbons with graphene edge-rich inner surfaces [7] by this principle. These carbon materials exhibit crystal structures that reflect the original supramolecular assemblies, which can be covalently captured by heating.

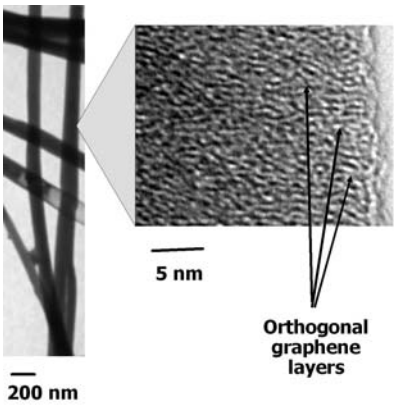

Figure 1. Orthogonal carbon nanofibers from discotic naphthalene polymer (AR mesophase).

In this paper we demonstrate the extension of this technique for producing novel hollow forms through solvent processing. Infiltration of polyaromatic solutions into nanochannel alumina followed by solvent evaporation coats thin organic films on the inner wall surfaces that can be covalently captured in the form of sp^2-hybridized carbon structures. Here our goal is to use nanochannels not only to dictate overall nanomaterial shape by the negative replica concept, but also to direct the molecular structure of the material through polyaromatic/alumina surface interactions.

Experimental

Two carbon precursors, (a) the solutions of naphthalene polymer (AR mesophase, HP grade from Mitsubishi Gas Chemical) in strong aromatic solvents, pyrindene and quinoline, and (b) indanthrone disulfonate (ammonium salt) aqueous solutions, were utilized in the experiment. In indanthrone disulfonate solutions, face-to-face stacking of the amphiphilic discotic molecules is extensive, leading to rod-like aggregates of ~ 1.5 nm in diameter and about 300 nm in length [8]. At high concentrations these solutions form lyotropic liquid crystalline phases in which the rod-like aggregates align by self exclusion and electrostatic repulsion [8].

Carbon nanoforms were produced by capillary infiltration of precursor solutions into nanochannel alumina followed by overnight drying and slow heating (4 °C/min) to 700 °C for 4 hours. The 700 °C treatment converts the organic nanotubes into monodisperse carbon tubes of 100 nm radius and 60 μm length, which form free standing ordered arrays upon removal of the alumina template by NaOH etching (see Fig. 2A). The resulting nanomaterials were then washed thoroughly and dried. SEM (scanning electron microscopy), TEM (transmission electron microscopy), and HRTEM (high-resolution TEM) were applied for morphology and structural analysis.

Results and discussion

Figures 2 shows the SEM images of carbon nanotubes and ribbons produced from indanthrone disulfonate. Using 12 wt-% indanthrone disulfonate solutions, the tubes show a cellular structure with hollow cavities separated by internal membranes (see Fig. 2A). This "bamboo" structure can be suppressed almost entirely by reducing solvent concentration from 12% to 2% to produce primarily hollow tubes with corresponding thinner walls (see Fig 3A).

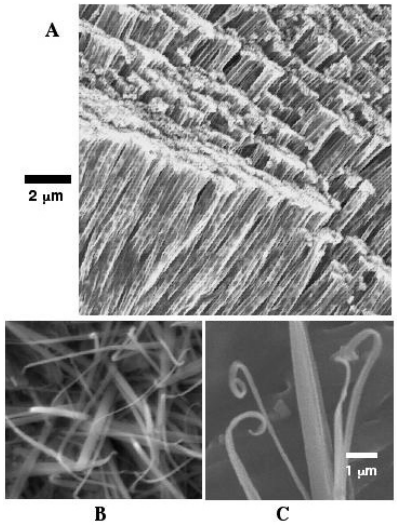

Figure 2. Carbon nanotube array (A) and dispersed nanoribbons (B, C) formed by capillary infiltration of indanthrone disulfonate solutions.

Dipping the filled nanochannel membrane in 10 wt% $BaCl_2$ solutions prior to drying and carbonization leads not to tubes but to nanoribbons — continuous carbon strips of 60 μm in length, 200 nm in width with rectangular cross section (Fig. 2 B,C). The divalent barium ion cross-links the negatively charged aggregates and reduces the solubility of the rod-like aggregates leading to

early precipitation *within* the nanochannels rather than deposition on wall surfaces.

High resolution fringe images (see Fig. 3) reveal a unique crystallography in these thin-walled carbon nanotubes, in which the graphene layers orient *perpendicular* to the tube axis. These meandering graphene layers are typical for a low-temperature carbon derived from a liquid crystal precursor [3, 6], and reflect the structure of the liquid crystalline phase at the point of solidification. The key feature in Fig. 3 is the uniform perpendicular alignment, which establishes the unique crystal orientation of this nanomaterial. Heat treatment of these phases can coalesce the layers and produce longer and straighter fringes, but does not alter the basic crystal symmetry set in the low-temperature carbon material [3].

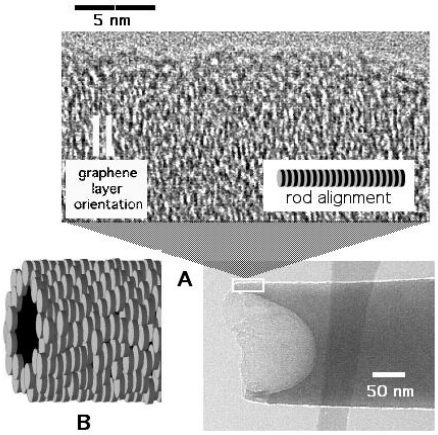

Figure 3. High-resolution TEM image of carbon nanotubes made from indanthrone-disulfonate. (Molecular disk size is B exaggerated for visibility).

We believe this unique crystal structure is formed by orientational ordering of the rod-like supramolecule aggregates driven by configurational entropy as the rods concentrate in the curved thin liquid films that coat the inner nanochannel walls. The dried solid film is then covalently captured by thermal polymerization with accurate translation of the molecular order into an arrangement of linked graphene layers.

Figure 4 shows the results for the other polyaromatic precursor---naphthalene polymer. The cylindrical carbon nanofoams have a similar graphene layer arrangement to the indanthrone-derived tubes, which shows a strong preferential alignment *perpendicular* to the tube axis. It is remarkable that both precursors give this unusual structure, which suggests some general principle in polyaromatic assembly. In fact the same basic perpendicular symmetry is observed when AR naphthalene polymer is melt processed in nanochannel alumina into fully dense fibers [6]. We believe that the driving force for assembly of these structures is the preservation of internal π-bonds, which are the strongest non-covalent interactions among large polyaromatics [3]. The molecular structure shown in Fig. 4 (massive axial π-stacked columns) achieves the maximum extent of internal π-bonding by exposing only graphene edges at the outer and inner wall surfaces. Further, the axial orientation of the columns avoids nanoscale curvature in the tangential direction. By this mechanism, large planar polyaromatic precursors provide a natural route to new carbon forms with edge-rich surfaces, provided that the supramolecular order can be captured upon heating.

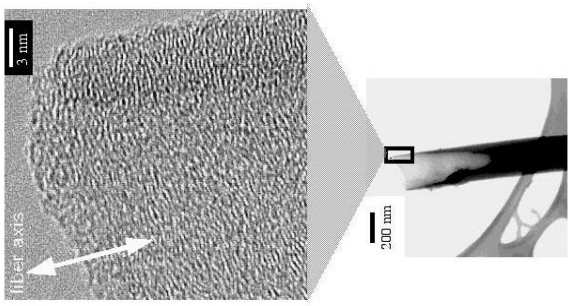

Figure 4. Perpendicular graphene layer arrangement in carbon nanotubes made from high-concentration solutions of naphthalene polymer in pyridine.

Conclusions

Polyaromatic solution processing can produce a unique set of cylindrical carbon nanoforms (tubes, ribbons) depending on synthesis conditions. The tubes and foams are crystallographically inverted and thus quite distinct from "conventional" carbon nanotube structures [1,9,10]. They exhibit graphene edge planes at both inner and outer surfaces and are interesting for a variety of applications where high-activity surfaces or access to interlayer spaces are advantageous.

Acknowledgements. This work was supported by the National Science Foundation through a Nanoscale Interdisciplinary Research Team (NIRT) Grant, CMS-0304246.

References

(1) Harris, P.J.F. Carbon Nanotubes and Related Structures, Cambridge University Press: Cambridge, **2001**.
(2) Ajayan, P.M. Ch. 8 in *Handbook of Nanostructured Materials and Nanotechnology, Vol 5: Organics, Polymers, and Biological Materials* (H.S. Nalwa Ed.) Academic Press, N.Y. **2000**.
(3) Hurt, R.H.; Chen, Z-Y. *Physics Today*, **2000**, 53(3), 39.
(4) Hurt, R.H.; Krammer, G.; Crawford, G.; Jian, K.; Rulison, C.; *Chem. Mater*, **2002**, 14, 4558.
(5) Jian, K.; Shim, H.S.; Tuhus-Dubrov, D.; Woodward, C.; Bernstein, S.; Pfeffer, M.; Steingart, D.; Sachsmann, S.; Gournay, T.; Crawford, G.P.; Hurt, R.H. *Carbon*, **2003**, 41 (11), 2073.
(6) Jian, K., Shim, H.-S., Schwartzman, A., Crawford, G.P., Hurt, R.H., *Adv. Mater.*, **2003**, 15 (2), 164-167.
(7) Yang, N.Y.C.; Jian, K.; Kulaots, I.; Crawford, G.P.; Hurt, R.H; *J. Nanosci. Nanotech* **2003**, 3 (5), 386.
(8) Dembo A. *Mol. Mater.*, **2001,** 14, 275.
(9) Iijima, S. *Nature*, **1991,** 354, 56.
(10) Kyotani, T.; Tsai, L.; Tomita, A. *Chem. Mater.*, **1995**, 7, 1427.

LARGE-SCALE SYNTHESIS OF HIGH-QUALITY DOUBLE-WALLED CARBON NANOTUBES FROM COAL-BASED CARBON RODS IN VACUUM BY ARC DISCHARGE

Jieshan Qiu[a],Yongfeng Li[a], Yunpeng Wang[a], Fayu Wu[b], Huiming Cheng[b], Guobin Zheng[c] and Yasuo Uchiyama[c]*

[a] Carbon Research Laboratory, School of Chemical Engineering, Center for Nano Materials and Science, Dalian University of Technology, 158 Zhongshan Road, P.O .Box 49, Dalian 116012, China. E-mail: **jqiu@dlut.edu.cn**; Fax: +86-411-8363-3080

[b] Shenyang National Labratory for Materials Science, Institute of Metal Research, CAS, Shenyang 110016, China.

[c] Department of Materials Science and Engineering, Nagasaki University, 1-14 Bunkyo-machi, Nagasaki 852-8521, Japan

Introduction

Since the first report about the preparation of double-walled carbon nanotubes (DWNTs) [1], great efforts have been made to their synthesis. The driving force behind this is because DWNTs consist of two concentric cylindrical graphene layers, which endows the DWNTs with some novel physical properties that are not found in other types of carbon nanotubes. For example, DWNTs can offer excellent field emission properties, which have low threshold voltage for electron emission like SWNTs and high durability similar to MWNTs. Up to now, several methods have been developed to synthesize DWNTs, which includes stable arc discharge,[2-4] pulsed arc discharge,[5] coalescence of C_{60} and catalytic chemical vapor deposition (CCVD).[6-11] Though some progresses have been made in the synthesis of DWNTs, it is still difficult to obtain pure DWNTs (without other forms of carbon materials such as the presence of SWNTs), and the production of cheap DWNTs in large quantity is still a challenge. Of those available techniques, the arc discharge is simple, cheap and easy to operate, and has some advanctages in production of DWNTs with high purity.

Here we report that it is possible to synthesize high-quality DWNTs in large quantity from coal-based carbon rods with Fe as catalyst by arc discharge in vacuum. Unlike the reported conventional arc techniques for synthesis of DWNTs, [2-4] our approach does not need buffer gas that is indispensable in conventional arc discharge.

Experimental

Carbon rods prepared from coal and iron powders was used as the anode in the arcing experiments. To make the carbon rods, the coal powder (*ca.* 150 μm) was first finely mixed with binder (coal tar) and iron powder (*ca.* 120 μm) in a weight ratio of 30% and 5%, respectively. The mixed paste was subsequently pressed at about 10-20 MPa to form composite coal rods. The coal rods were then put into an electric furnace and carbonized in flowing Argon to make composite carbon rods with a diameter of *ca.* 10 mm. The composite carbon rods were used as the anode in arc discharge, while a high purity graphite rod with a diameter of 16mm was made as the cathode. Before arcing, a wire cage was put inside the reactor for direct collecting the as-formed DWNTs, of which the detailed information can be found elesewhere.[12] The arc-discharge was conducted with a DC of 60-70 A and a voltage of 40-50V in low vacuum (only 0.001~0.01Pa of air). The typical arcing experiment normally lasted for about 5~7 min. After arc discharge, the wire cage was taken out, of which the surface was covered with web-like deposits that were directly peeled off and examined by scanning electron microscopy (SEM, JSM-5600LV), transmission electron microscopy (TEM, JEOL 2010) and Raman spectroscopy (Jobin Yvon LabRam HR 800, excited by 623.8 nm laser).

Results and Discussion

Figure 1 shows macroscopic web-like DWNTs deposited on the wire cage. The repeated experiments show that for the vacuum approach with iron-containing coal-based carbon rods as starting carbon source, the production rate of DWNTs varies in arange of 20~25 mg/min.

Figure 1. Macroscopic image of web-like DWNTs, formed on the wire cage by vacuum arc discharge.

Typical SEM images of DWNTs peeled off from the wire cage are shown in Figure 2. The SEM results indicate that most of products appear in a uniform film-like morphology, as can be seen in Figure 2a, or in well-aligned thread-like morphology, as shown in Figure 2b, which is quite similar to the morphology of film-like SWNTs.[12] But the DWNTs film is less sticky compared with the SWNTs films.

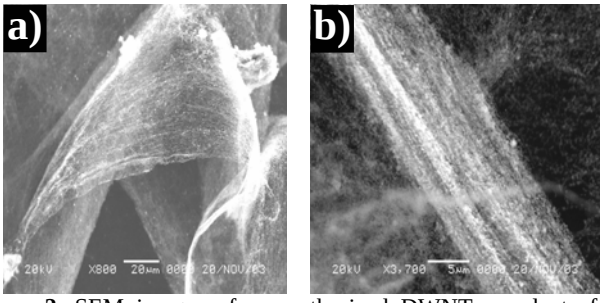

Figure 2. SEM images of as-synthesized DWNTs products from coal-based carbon rods under vacuum arcing conditions, (a) film-like DWNTs, (b) aligned thread-like DWNTs.

The as-synthesized DWNTs samples were further examined by TEM, which confirms that DWNTs dominate in the products with the content being over 95%, and only a few SWNTs are present, no MWNTs is found. This significantly differs from the DWNTs prepared by traditional arc discharge or CCVD methods, of which only about 90% are DWNTs even under the optimum preparation conditions. Figure 3a shows some isolated DWNTs and most of them have a smooth surface and average outer diameter of 4-5 nm. A typical DWNTs bundle usually consists of 4 to 10 individual nanotubes, as can be seen in Figure 3b. Figure 3c is a high-magnification TEM image, showing two double-walled nanotubes with the interlayer spacing being *ca.* 0.40nm in the section as the arrows indicates. Figure 3d shows a DWNTs bundle consisting of 4 DWNTs, of which the average outer diameter is *ca.* 4.2 nm. It should be noted that the DWNTs in bundles seem to have a smaller diameter than those isolated DWNTs.

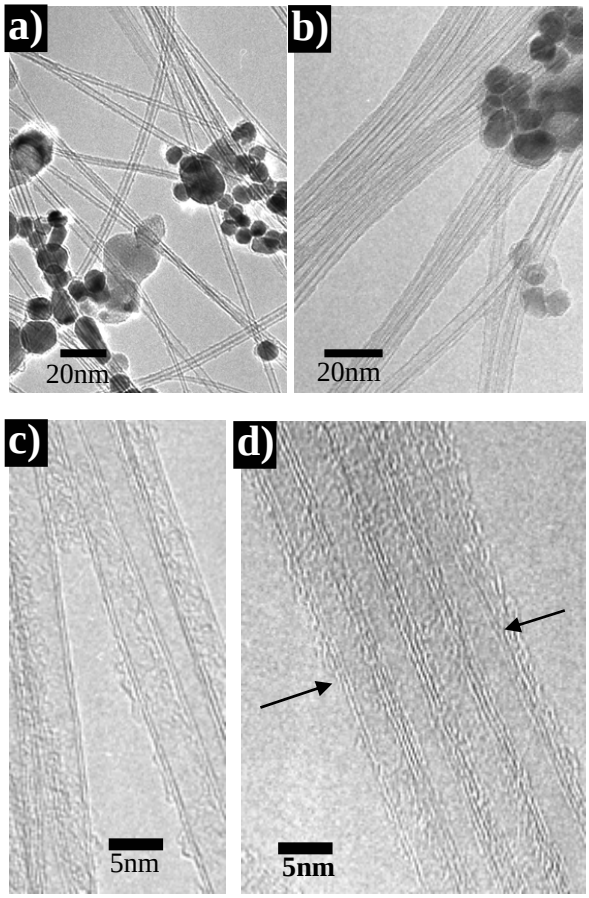

Figure 3. TEM images of DWNTs obtained from coal-based carbon rods with Fe as catalyst under vacuum arcing conditions, (a) and (b), low magnified images, showing some isolated and bundle-like DWNTs, (c) two isolated DWNTs and (d) four DWNTs joining together to form a bundle.

Raman spectroscopy was also used to characterize the obtained DWNTs, which yields some information about the diameter of as-prepared DWNTs. It is necessary to mention that carbon nanotubes with a diameter over 3 nm exhibit a weak Raman signal, and their radial breathing mode (RMB) band is difficult to detect.[2,8] The HRTEM studies discussed above reveal that most of the DWNTs have an average diameter around 4.0-5.0nm, here the diameter distribution calculated according to Raman shift only represents those DWNTs with a diameter less than 3 nm. A typical DWNTs Raman spectrum in the range of 0-2000 cm^{-1} is shown in Figure 4, and the inset is the RMB in the low frequency range of 50-300cm^{-1}. In the Raman spectroscopy, a weak D-band at 1325.6 cm^{-1} and a strong G-band at 1584.5cm^{-1} can be seen. The weak D-band means that the DWNTs products is high-purity nanotube material, while the high value of G/D imply that the content of the disordered or defective graphitic structure in the DWNTs nanotubes is low, which is consistent with the SEM and TEM observation. The diameter of DWNTs is calculated by the well-known expression $\omega_r = 238/d^{0.93}$, where d is diameter of tubes in nm and ω_r is the frequency of RMB in cm^{-1}. [13] The peak positions between 101.8 and 219.6cm^{-1} correspond to the presence of carbon nanotubes with diameter between 2.49 and 1.09 nm. The two pair peaks at position of 131.9 and 219.6cm^{-1} reveal that some DWNTs have outer diameter of 1.89nm and inner diameter of 1.09nm.

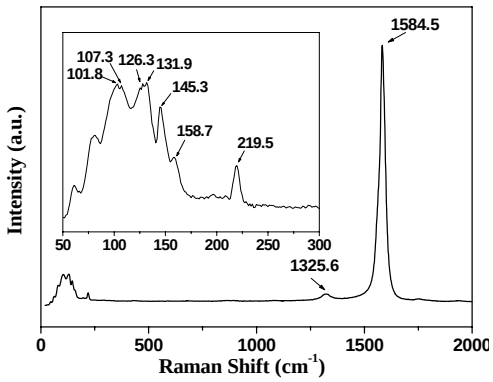

Figure 4. Raman spectra of DWNTs synthesized from coal-based carbon rods under vacuum arcing conditions, the inset showing RMB band of DWNTs below 300 cm^{-1}

In summary, a large amount of DWNTs with high quality have been successfully synthesized from coal-based carbon rods by arc discharge under vacuum conditions. Most of DWNTs have an outer diameter of 4-5 nm and a small amount of them have a diameter less than 2 nm. Our results demonstrate for the first time that it is possible to prepare high quality DWNTs with a diameter of 4.0-5.0 nm from coal-based carbon rods without any inert buffer gas, this approach may become an favorable option for making high quality DWNTs with bigger diameters.

Acknowledgment. This work was partly supported by the National Science Foundation of China (No. 29976006, 20376011), the Natural Science Foundation of Liaoning Province (No. 9810300701, 2001101003), the National Basic Research Program of China (Grant No. G2003CB615806) and the Ministry of Education of China.

References

(1) Hutchison J.L.; Kiselev N.A.; Krinichnaya E.P.; et al. *Carbon*, 2001, 39, 761.
(2) Saito Y.; Nakahira T; and Uemura S. *J. Phys. Chem. B*, 2003, 107, 931.
(3) Huang H.; Kajiura H.; Tsutsui S.; et al. *J. Phys. Chem. B*, 2003, 107, 8794.
(4) Sugai T.; Yoshida H.; Shimada T.; Okazaki T.; Shinohara H.; *Nano Lett.,* 2003, 3, 769.
(5) Colomer J.F.; Henrard L.; Flahaut E.; Tendeloo G.Van; Lucas A.A.; Lambin Ph.; *Nano Lett.,* 2003, 3, 685.
(6) S. Bandow, M. Takizawa, K.Hirahara, M.Yudasaka and S. Iijima, *Chem. Phys. Lett.*, 2001, 337, 48.
(7) Ren W.; Li F.; Bai S.; Cheng H.M.; *Chem. Phys. Lett.*, 2002, 359, 196.
(8) Ci L.; Rao Z.; Zhou Z.; Tang D.; Yan X.; Liang Y.; Liu D.; et al. *Chem. Phys. Lett.*, 2002, 359, 63.
(9) Lyu S.C.; Lee T.J.; Yang C.Y.; Lee C.J.; *Chem. Comm*, 2003, 1404.
(10) Flahaut E.; Bacsa R.; Peigney A.; Laurent Ch.; *Chem. Comm*, 2003, 1442.
(11) Qiu J.S.; Li Y.F.; Wang Y.P.; Wang T.H.; Zhao Z.B.; Zhou Y.; Li F.; Cheng H.M.; *Carbon*, 2003, 41, 2159.
(12) Ci L.; Zhou Z.; Yan X.; Liu D.; Yuan H.; et al. *J. Phys. Chem. B*, 2003, 107, 8760.

COAL-DERIVED HOLLOW CARBON CAPSULES WITH INNER DIAMETER OVER 40 NANOMETERS: GIANT MULTISHELL FULLERENES?

Jieshan Qiu, Yongfeng Li, Xiuna Wang, Zongbin Zhao

Carbon Research Laboratory, Center for Nano Materials and Science, State Key Laboratory of Fine Chemicals, Dalian University of Technology, 158 Zhongshan Road, P.O .Box 49, Dalian 116012, China. E-mail: jqiu@dlut.edu.cn

Introduction

After the macroscopic preparation of fullerenes (C_{60}) in 1990,[1] a number of nano-sized novel carbon materials including nanotubes(CNTs), carbon onions, carbon horns, multishell fullerenes, graphite polyhedral crystals, tubular graphite cones and other nano-sized carbon particles [2-10] have been found. The morphology and properties of these novel carbon nanomaterials are closely related to the techniques and the carbon precursors used. One of the techniques widely used is the arc discharge method, in which high purity graphite or composite graphite electrodes are normally used as carbon precursor. However, when coal, one of the cheapest carbon sources in nature, is used instead of expensive graphite, various forms of carbon nanomaterials such as fullerenes, multi-walled CNTs and single-walled CNTs can also be prepared. [11-18] It is believed that the unique chemical structure of coal and coal-based carbons plays a key role in the formation of various novel carbon nanomaterials. Here we report the synthesis of a novel form of carbon capsules with a nano-sized hollow central cavity by arc discharging coal-based iron-containing carbons. The size distribution of these hollow carbon capsules (thereafter called HCCs) is quite uniform with outer diameters around 50-70nm and inner diameters around 40nm.

Experimental

The conventional DC arc-discharge method was used to prepare giant hollow carbon capsules (HCCs) with the coal-derived carbon rods as the anode. The coal sample used is an anthracite coal, and its proximate and ultimate analyses can be found elsewhere.[17] The coal-derived carbon rods were prepared according to the following procedure. The coal powder (less than 150μm) was mixed with coal tar in a weight ratio of 20% and then pressed in a mold to form coal tubes (10 mm o.d., 5mm i.d. and 120mm in length). Then, the coal tubes were put into an electric furnace and heated at a heating rate of 10 ^{o}C/min till 900 ^{o}C in flowing N_2. The tubes were kept at 900^{o}C for 4 h before being cooled back to room temperature to get carbon tubes. Some tubes were crushed to make char powders (less than 150μm) which were mixed with iron powders (less than 150μm) in a weight ratio of 50:50. The mixture was packed into the carbon tubes, of which both ends were sealed with graphite plugs. The coal-based carbon rods were subjected to electrical arcing, which was conducted in He with an initial pressure of 0.065MPa. The arc was generated between the coal-derived anode and a graphite cathode (16 mm in diameter) with a current of 50-70A and a voltage of 30-50V. The arcing experiments normally lasted about 20 min. After the arc-discharge was finished, three types of products were collected in different parts inside the arc-reactor chamber: fullerenes-containing soot deposited on the inner walls; hard and gray deposits on the tip of cathode and fiber-like black deposit on the periphery of the end of coal-based anode. All these three types of the products were examined by TEM (JEM-2000EX, operated at 100kV). The samples were sonicated in ethanol for 5 min before being dropped onto a copper grid for TEM examination. It is in the fiber-like black deposits on the periphery of the end of coal-based anode that the HCCs was found.

Results and Discussion

The typical TEM images of HCCs are shown in Figure 1, from which bamboo-shaped CNTs (as shown in Fig. 1a) and normal multi-walled CNTs (as shown in Fig. 1b) can also be seen occasionally. This means that the HCCs are formed spontaneously with CNTs, and this leads one to believe that they might be an intermediate product between small carbon molecules (fullerenes) and giant carbon molecules such as the bamboo-shaped CNTs shown in Fig. 1a. Some of the HCCs have a perfect ball-like shape or core–shell morphology as shown in Fig. 1c and some have, to some degree, a distorted or elongated ring-like shape, which may be due to the fluctuations of the concentrations of the active carbon particles that were released from coal-based carbon rods by arcing discharge and directly incorporated into the HCCs. It is interesting to note that there is a similarity between the conical caps of the hollow compartments in the bamboo-shaped nanotube and the hollow carbon capsules (HCCs), which can be easily visualized that if one of the HCCs were cut into two halves, one half would make a rather perfect cone-shaped cap of the hollow compartment in the bamboo-shaped nanotube, as shown by arrows in Fig. 1a. This analogy leads one to believe that both the HCCs and the bamboo-shaped carbon tubes start to grow from the same precursors. It is known that small fullerenes molecules can coalesce to form larger ones. For example, Mochida et al[19] has shown that heat treatment of C_{60} at high temperature (up to 2400 ^{o}C) resulted in the formation of fullerene-like nanoparticles with diameters in a range 5~15nm. With these in mind, the observations discussed above could also lead one to speculate that at the high temperature (~3000^{o}C) of the arc plasma, the HCCs might be the intermediate species in the growth process of the bamboo-shaped nanotubes.

On average, these novel HCCs have an outer diameter around 50-70nm and an inner diameter around 40-50nm. It is estimated that for these HCCs, the volume ratio of the inner space to the whole particle is about 30-52%, which is far greater than 1% for the conventional polyhedral carbon particles described in literature. [4] It is interesting to note that similar to C_{60}-type fullerenes, the central cavity of these HCCs are totally empty and none of them is filled with metal particles or metal carbides.

The purity of HCCs is very high, as shown in Fig. 1c-1e. From the TEM images, it has been estimated that the content of the giant HCCs in the deposits at the end of anode may reach up to 80-90%. It is known that polyhedral carbon nanoparticles with large central cavity are not stable under electron bombardment. [3,7] This is also the case for HCCs. During the TEM examination, some HCCs would collapse and lose part of their inner empty space, as indicated by the arrows in Fig. 1d. This happened frequently when we were trying to focus the microscopy to get a clear image of the HCCs in spite of the low operation voltage of 100kV.

An analogy can be made between the nano-sized hollow carbon capsules reported here and multishell fullerenes with a cage-inside-cage concentric structure that were foreseen by Kroto et al [20] shortly after the discovery of the fullerene C_{60}, and several multishell fullerenes such as double-shell $C_{60}@C_{240}$, $C_{240}@C_{560}$ and triple-shell $C_{60}@C_{240}@C_{560}$, $C_{80}@C_{240}@C_{560}$ were successfully prepared by laser vaporization of composite carbon-metal targets.[8] For the HCCs reported here that are structurally related to large and multishell fullerenes, pentagons and heptagons may have played a primordial role in their formation, which is similar to the formation of single-shell and multishell fullerenes as well as carbon nanotubes. [6,7]

Up to now, hollow carbon nanoparticles with much smaller inner central cavity are usually obtained by arc discharge of pure

graphite electrodes.[4,7] The graphite-derived nanoparticles usually display a polyhedral morphology with an inner empty space (3-10nm in diameter)[3,7] that is at least 4 times smaller than the inner diameter of the HCCs reported here. Those nanoparticles with large central cores tend to be more faceted than those with small inner shells and are frequently irregularly shaped with more than six sides.[7] In contrast to the traditional carbon nanoparticles, the HCCs obtained from coal-based carbon by arc discharge with iron as catalyst have two peculiar characteristics: a nearly perfect spherical shape and the inner diameter around 40-50nm that is much larger than that of the common polyhedral nanoparticles.

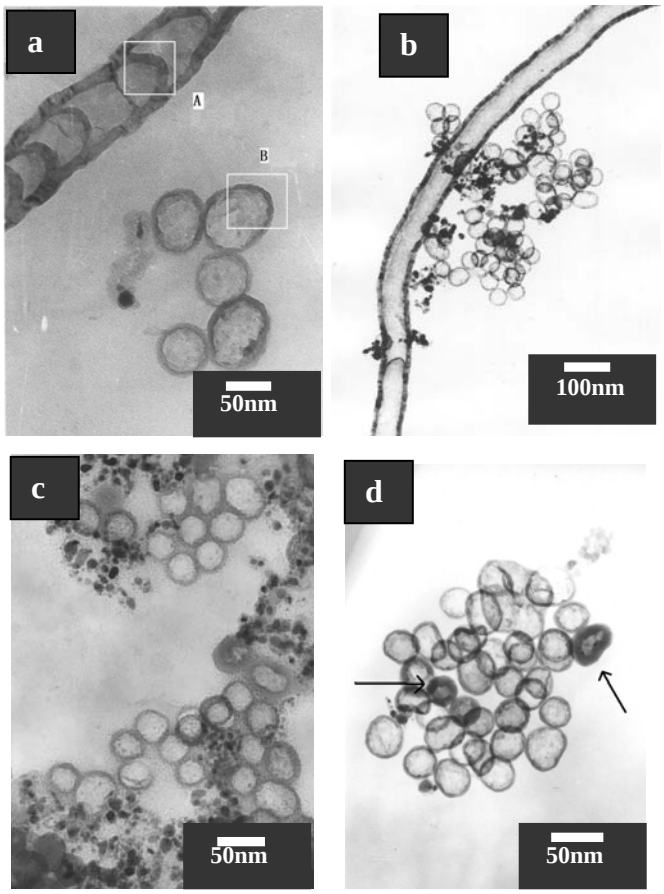

Figure 1. TEM images of hollow carbon capsules (HCCs) prepared from coal with Fe as catalyst, on the average, these HCCs have a quite uniform particle size, with outer diameters around 50-70nm and inner diameters around 40-50nm; (a) five HCCs accompanied with a bamboo-shaped carbon nanotube; (b) many HCCs accompanied with a long multiwall carbon nanotube; (c) and (d) TEM image showing most of the HCCs with almost perfect sphere-like shape.

The formation mechanism of these HCCs is not clear at the moment, nevertheless it must be related to the chemical structure of coal-based carbon and the presence of Fe metal. It is well known that the chemical structure of coal-based carbons is very complex and resembles graphite crystalline in the domain of 1-10 nm in which the basic units are small graphitic crystallites containing a few layer planes. These small graphitic crystallites are joined together by relatively weak crosslinks that would break first under arcing conditions to release some of the small graphitic crystallites (termed as SGCs thereafter) as free particles, and some of them might be directly incorporated into HCCs without going atomization as in the case of graphite process in which the graphite sheets need to be first decomposed into C_1 or C_2 species,[6,7,12] but it should be noted that the SGCs might go further decomposition to result in a large amount of aromatic specie such as polycyclic aromatic hydrocarbons (PAHs) and C_1 or C_2 species, which then take part in the formation reaction of HCCs as the basic building blocks in the presence of Fe metal particles. It is known that iron group metals are good catalysts for carbon graphitization reactions and for CNTs preparation, thus Fe metal particles or atoms might be responsible for catalyzing the formation of the HCCs.

For comparison, the arc-evaporation of iron-filled graphite anode was also conducted under the same arcing conditions, with a hope to get some indirect evidence that will help us to understand how these HCCs are formed. The high purity graphite electrode was first drilled to make a hole for filling the same iron particles as in the case of coal-based carbon tubes, but no HCCs were found. This indicates, indirectly and clearly, that the formation of HCCs is due to the peculiar chemical structure of coal-based carbon, though the detailed mechanism involved in the formation process is not known.

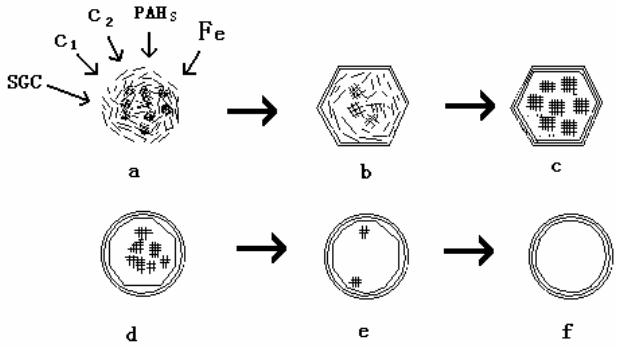

Figure 2. Schematic illustration of the growth stages of HCCs; (a) the initial stage in which a mixture consisting of molten Fe metal particles and various carbon species such as small graphitic crystallites (SGCs) and polycyclic aromatic hydrocarbon (PAHs) as well as C_1/C_2 species is formed. The mixture may be in liquid phase or quasi-liquid phase; (b) graphitization begins from the surface of the particles induced by Fe catalyst. (c-e) Fe metal particles are driven out of the shells leaving the empty capsule behind, at the same time, the polyhedral shape is gradually transformed into a quasi-spherical one because of the high-energy electron irradiation and high temperature in the arc plasma. (f) well-developed hollow carbon capsules are formed.

To understand the nature of how the HCCs are formed, a model is proposed to explain the growth process of the HCCs, in which the roles played by SGCs, PAHs, C_1 or C_2 species and Fe metal particles are all taken into account, which is schematically shown in Fig. 2. The first step for the growth of HCCs is the formation of clusters consisting of the molten Fe metal particles and the aromatic carbon species such as SGCs and PAHs as well as the C_1 or C_2 species. The carbon species are released from the coal-based carbon rod that is vaporized in arc plasma of high temperature (*ca.* 3000°C). In the initial stage (Fig. 2a), the mixture consisting of various carbon species and Fe metal particles may be in liquid phase or quasi-liquid phase. Then, the formation of graphitic carbon layers starts due to the catalytic effect of Fe metal and the high temperature, as shown in Fig. 2b and 2c. Since the outer periphery of the particles will likely consist of larger, more favorably oriented layers [20] that possess fewer

energetic and structural barriers to realignment and growth than those in the inner interior, the growth of graphitic layers is supposed to start on the outer surface and progress toward the center [3]. It is known that the melting point of carbon is much higher than Fe, thus, the initial density of carbon in the particle or cluster should be lower than pure carbons. In other words, the vapor pressure of Fe is much higher than carbon, which causes Fe atoms evaporate through the defects of the outer graphitic carbon layers, in the stage (c) to (e), as shown in Fig. 2c-2e. At the same time, the transformation of polyhedral shape into a quasi-spherical one also takes place due to the high-energy electron irradiation and high temperature in the arc plasma zone, which leads to the HCCs with perfect sphere shape, as shown in Fig. 2f. It is worth noting that none of the HCCs obtained in this way is filled with Fe particles or other elements. This might be due to the fact that the starting building blocks of the HCCs mainly consist of the large aromatic species such as the SGCs and PAHs species rather than the small units such as C_1 and C_2 species as in the case of arc-evaporation of graphite. This may account for why the formed HCCs have a big inner diameter. For some unknown reasons, the coalescence of large aromatic carbon species would lead to relatively more defects in cage shells during the growth from stage (b) to stage (e), as shown in Fig. 2, which makes the Fe being easily driven out of many shells and leaving the empty capsules behind, as shown in Fig. 2f.

Conclusions

In summary, a novel form of hollow carbon capsules (HCCs) have been prepared from coal-based carbon by arc discharge with iron as catalyst. These HCCs have a uniform size distribution with outer diameters around 50-70nm and inner diameters around 40-50nm. The growth mechanism of this novel HCCs has been discussed in terms of the chemical structure of coal-based carbon and the arcing discharge conditions.

Acknowledgment. This work was partly supported by the National Science Foundation of China (No. 29976006, 20376011), the Natural Science Foundation of Liaoning Province (No. 9810300701, 2001101003), the National Basic Research Program of China (Grant No. G2003CB615806) and the Ministry of Education of China.

References

(1) Kratschmer, W.; Lamb, L.D.; Fostiropoulos, K.; Huffman, D.R.; *Nature.* **1990,** 347, 54.
(2) S. Iijima, *Nature* **1991**, 354, 56.
(3) Ugarte, D.; *Carbon.* **1995**, 33, 989.
(4) Saito, Y.; *Carbon.* **1995**, 33, 979.
(5) Saito, Y.; Nishikubo, K.; Kawabata, K.; Matsumoto, T.; *J. Appl. Phys.* **1996**, 80, 3062.
(6) Dresselhaus, M.S.; Dresselhaus, G.; Eklund, P.C.; *Science of Fullerenes and Carbon Nanotubes*, Academic Press, London, **1996**.
(7) Harris, P.J.F.; *Carbon Nanotubes and Related Structures*, Cambridge University Press, **1999**.
(8) Mordkovich, V.Z.; Takeuchi, Y.; *Chem. Phys. Lett.* **2002**, 355, 133.
(9) Gogotsi, Y.; Libera, J.A.; Kalashnikov, N.; Yoshimura, M.; *Science*. **2000**, 290, 317.
(10) Zhang, G.Y.; Jiang, X.; Wang, E.G.; *Science.* **2003**, 300, 472.
(11) Pang, L.S.K.; Vasslalo, A.M.; Wilson, M.A.; *Nature.* **1991**, 352, 480.
(12) Wilson, M.A.; Patney, H.K.; Kalman, J.; *Fuel.* **2002**, 81, 5.
(13) Qiu, J.S.; Zhou, Y.; Wang, L.N.; Tang, S.C.; *Carbon.* **1998**, 36, 465.
(14) Qiu, J.S.; Zhou, Y.; Yang, Z.G.; Wang, L.N.; Zhang, F.; Tsang, S.C.; Harris, P.J.F.; *Molecular Materials.* **2000**, 13, 377.
(15) Qiu, J.S.; Zhou, Y.; Yang, Z.G.; Wang, D.K.; Guo, S.C.; Tsang, S.C.; Harris, P.J.F.; *Fuel.* **2000**, 79, 1303.
(16) Williams, K.A.; Tachibana, M.; Allen, J.L.; Grigorian, L.; Cheng, S.C.; Fang, S.L.; Sumansekera, G.U.; Loper, A.L.; Williams, J.H.; Eklund, P.C.; *Chem. Phys. Lett.* **1999**, 310, 31.
(17) Qiu, J.S.; Zhang, F.; Zhou, Y.; Han, H.M.; Hu, D.S.; Tsang, S.C.; Harris, P.J.F.; *Fuel.* **2002**, 81, 1509.
(18) Li, Y.F.; Qiu, J.S.; Zhao, Z.B.; Wang, T.H.; Wang, Y.P.; Li, W.; *Chem. Phys. Lett.* **2002**, 366, 544.
(19) Mochida, I.; Egashira, M.; Korai, Y.; Yokogawa, K.; *Carbon* **1997**, 35, 1707.
(20) Kroto H.W.; MaKay, K.; *Nature.* **1988**, 331, 328.
(21) Saito, Y.; Yoshikawa, T.; Okuda, M.; *Chem. Phys. Lett.* **1993**, 209, 72.

FLAME SYNTHESIS OF CARBON NANOTUBES USING CATALYST PARTICLES PREPARED BY LASER ABLATION

*Randy L. Vander Wal, Gordon M. Berger and Thomas M. Ticich**

The National Center for Microgravity Research (NCMR)
c/o The NASA-Glenn Research Center
M.S. 110-3
21000 Brookpark Rd.
Cleveland, OH 44135

* Centenary College of Louisiana
Dept. Of Chemistry
2911 Centenary Blvd.
Shreveport, LA 71134

Introduction

Carbon nanotubes and nanofibers are sought for many applications reflecting their novel mechanical, thermal and electrical properties including reinforcing, catalyst support, gas storage and electrochemical energy storage [1]. These applications will require bulk synthesis methods, producing ton quantities. Towards this goal, flame synthesis has demonstrated potential for producing nanoscale materials such as TiO_2, SiO_2 and carbon black on an industrial scale. Thus, we are pursuing flame synthesis for nanotubes and nanofibers.

Our previous work has shown a strong reactivity difference between Fe and Ni nanoparticles [2-4]. The metals manifest a high selectivity towards either CO or C_2H_2. Ni reacts with CO/C_2H_2 gas mixtures to produce nanofibers; whereas, Fe reacts with CO to produce SWNTs. The catalyst to product correlation is very high. Fe has not been observed to catalyze MWNTs nor nanofibers, and Ni has not been observed to catalyze SWNTs.

Moreover, these metals also demonstrate a different onset of catalytic activity. Previous studies used in situ catalyst particle formation using nebulized metal salt solutions. To avoid the complex chemistries involved in this process and directly study the highly selective reactivities of these different metals, the onset of catalytic activity and the potential associated particle size effects, laser ablation was used to generate the metal nanoparticles [5].

Experimental

Laser ablation was used to create the catalyst nanoparticles of Fe or Ni. As aerosols, the nanoparticles were entrained within a gas flow and introduced into the central tube within a custom, McKenna premixed burner. Apart from the premixed flame, whose composition could be varied but was maintained constant for these experiments, gas mixtures through the central tube of the burner consisted of CO/H_2/He/C_2H_2 mixtures, with each gas controlled independently and regulated by mass flow controllers or rotameters. Further details of the burner, operating conditions and TEM microscopy have been reported previously [2-4].

The water-cooled burner was operated using a rich premix of acetylene and air. Fuel-air equivalence ratios were 1.5 to 1.55, produced using an acetylene flow rate of 1.5 slpm and an air flow rate ranging from 11.3 to 11.5 slpm. A 3 inch long, 1 inch OD quartz chimney served to stabilize the post-combustion flame gases against buoyancy-induced flicker and guided the metal aerosol and associated reaction gases as a laminar flow. Samples of the metal-catalyzed products were collected by thermophoretic sampling directly upon lacey TEM grids above the chimney for analysis.

Results and Discussion

Onset of catalytic reactivity and selectivity based on gas identity. Fe reacted in both the CO and CO/C_2H_2-based gas mixtures, producing SWNTs. Fig. 1 shows TEM images of these products at various magnifications. In contrast, Ni was unreactive towards the CO gas mixture. It only reacted with the CO/C_2H_2 gas mixture, producing nanofibers. This is shown in the TEM images of Fig. 2.

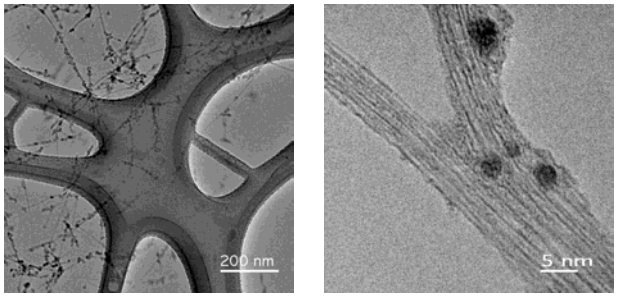

Figure 1. TEM images of SWNTs, shown as sampled from the flame, using Fe as the catalyst.

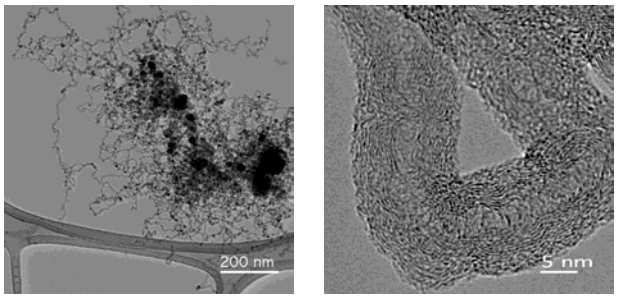

Figure 2. TEM images of nanofibers, shown as sampled from the flame, using Ni as the catalyst.

Ni. A greater yield of nanofibers of greater length were produced with the the CO/C_2H_2 based gas mixture than with C_2H_2 alone. Moreover, the reactivity of Ni towards C_2H_2 (at the same concentration) in the absence of CO appears to be increased, where fewer nanofibers, of shorter lengths were produced (along with encapsulated particles). Not only do these results suggest that C_2H_2 serves as the main carbon supply for Ni-catalyzed nanofibers, but that CO plays an inhibitory role in that its adsorption and associated slower reactivity restricts the rate of C_2H_2 adsorption (by site blockage), and hence, slows the rate of carbon supply. Our results also suggest that ultrasmall Ni particles (< 4 nm) may not be particularly active towards catalyzing C_2H_2 dissociation. Finally, there is an absence of SWNTs catalyzed by Ni with either C_2H_2 or CO/C_2H_2 gas mixtures. Ultrasmall Ni nanoparticles may not be sufficiently reactive. Therein, it appears that the onset of catalytic activity of Ni for nanotube synthesis is attained only by larger particles, beyond a minimum size of roughly 4 nm. Upon reaching this size range, the catalyst particles are too large for SWNT synthesis. Instead, they catalyze nanotubes or nanofibers.

Fe. On the basis of bulk crystal studies, Fe is considered to be more reactive than Ni [6]. Clearly, it achieves an earlier onset of reactivity, as only the very smallest Fe particles catalyze nanotubes, in this case SWNTs. Therein, Fe might be expected to readily react with C_2H_2, particularly since it reacts with CO. One might even predict that CO, as a less reactive carbon source could yet play a similar role in restricting the rate of carbon supply through C_2H_2 dissociative adsorption, as it does with Ni. The difference here is that it would also contribute to the carbon supply. Yet further tests show that Fe exhibits selective reactivity towards CO. Moreover, the absence of nanofibers of MWNTs suggests a decline in reactivity with increasing particle size for Fe nanoparticles, in contrast to Ni.

Metal Nanoparticles. For each molecule, dissociative adsorption involves both electron donation and withdrawal [7, 8]. Additionally, in a metal nanoparticle, the density of electronic states is finite and the traditional conduction and valence bands are absent due to the small number of constituent atoms [9, 10]. With > 75% of the atoms residing at the surface for a 1 nm particle, the particle properties will largely be determined by the surface atoms. This will be particularly true for those atomic orbitals not participating (contributing electron density) in the free conduction band of the metal, such as the 3d orbitals of the transition metals [6, 7]. If the electronic properties of a metal nanoparticle resembles those of the individual element, given the finite size and high surface area, then based on energetics associated with its outer electron configuration, $[Ar]5s^23d^6$, Fe atoms can achieve a stable half filled d-shell by loss of electron density such as by donation of electron density to an adsorbate, e.g. CO. In contrast, acceptance of electron density might be expected to be energetically unfavorable, given the increase in energy associated with pairing electron density within the d-shell orbitals. Therein, Fe would be expected to be unreactive towards C_2H_2.

The situation for Ni is exactly opposite. Adopting the premise that the individual elemental identity still (largely) governs the electronic properties of the surface atoms and hence, their reactivities, it would be energetically favorable for Ni to accept electron density to achieve a more stable, filled d-shell, namely $[Ar]5s^23d^{10}$. Therein, Ni would be expected to be highly reactive towards adsorbates which donate electron density, e.g. C_2H_2. Correspondingly, Ni would be unreactive towards adsorbates that accepted (withdrew) electron density from the metal nanoparticle, e.g. CO.

This exceedingly simple explanation certainly neglects several factors. First, it ignores the possible contribution of other adsorbates to the nanoparticle-adsorbate system. For example, bulk single crystal studies show that H_2 upon dissociative adsorption can donate electronic charge density to Fe [6, 11]. The preferential reactivity of Fe and Ni towards particular gases may also be related to steric effects which make a somewhat larger nanoparticle more accessible to species which adsorb in a sideways configuration (parallel to the nanoparticle surface like C_2H_2) rather than in an end-on configuration (such as CO) [11]. Undoubtedly, other factors such as thermal restructuring, adsorbate-enhanced restructuring and electronic interactions between adsorbates mediated by the catalyst particle are integral to these results.

Acknowledgements. This work was supported by a NASA NRA 97-HEDs-01 combustion award (RVW) administered through NASA cooperative agreement NCC3-975 with The National Center for Microgravity Research on Fluids and Combustion (NCMR) at The NASA-Glenn Research Center. The authors gratefully acknowledge Dr. Y. L. Chen and David R. Hull for the TEM imaging.

References

(1) *Carbon Filaments and Nanotubes: Common Origins, Differing Applications?* (Biro, L. P.; Bernardo, C. A.; Tibbetts, G. G.; and Lambin, Ph., Eds.), Nato Science Series, Kluwer Academic Publishers, Dordrecht, The Netherlands, **2001**, Vol. 372.
(2) Vander Wal, R. L., *Carbon*, **2002**, 40, 2101.
(3) Vander Wal, R. L., *Combust. and Flame*, **2002**, 130, 37.
(4) Vander Wal, R. L.; L. J. Hall, *Chem. Phys. Lett.*, **2001**, 178, 349.
(5) Gnedovets, A. G.; Kul'batskii, E. B.; Smurov, I; Flamant, G., *Appl. Surf. Sci*., **1996**, 96-98, 272.
(6) Somorjai, G. A.; Kim, C. M.; Knight, C., in "Surface science of catalysis: In situ probes and reaction kinetics", (Dwyer, D. J.; and Hoffman, F. M., Eds.) American Chemical Society, Washington DC, **1992**.
(7) Chemical Kinetics and Catalysis, (Van Santen, R. A.; and Niemantsverdriet, J. W., Eds.) Plenum Press Inc. New York, **1995**, Chp. 6
(8) Campbell, I. M., *Catalysis at Surfaces*, Chapman and Hall Inc., New York, **1988**, Chp. 5
(9) Zhang, J. Z., *Acc. Chem. Res.*, **1997**, 30, 423.
(10) El-Sayed, M. A., *Acc. Chem. Res.*, **2000**, 34, 257.
(11) Dry, M. E.; Shingles, T.; Boschof, L. J.; Van Botha, H. C. S., *J. of Catalysis*, **1970**, 17, 347.

IMMOBILIZATION OF CARBON NANOFIBERS (CNFs); A NEW STRUCTURED CATALYST SUPPORT

Nabeel A. Jarrah, Jan G. van Ommen and Leon Lefferts

Faculty of Science and Technology, IMPACT, University of Twente, P. O. Box 217, 7500 AE, Enschede, The Netherlands

Introduction

One of the main problems in reactions performed in liquid phase over solid catalyst is to avoid mass transfer limitation. Slow diffusion as well as frequent occurrence of low reactant concentrations (e.g. dissolved H_2 or O_2) are responsible for this, resulting in concentration gradients around and in catalyst particles. Variation of the local concentrations of reactants and products over the active sites affects both activity and selectivity and thereby frustrates optimization of the operation of such reactors.

The concentration gradient in a catalyst particle strongly depends on the size of the catalyst particle. Downsizing of catalyst particles is limited due to hydrodynamic constraints in trickle bed reactors and filtration problem in suspension reactors.

CNF are graphite materials, which can be catalytically produced by decomposition of a carbon containing gas over small metal particles like nickel. In many cases the fibers are strongly entangled, forming aggregates. These aggregates are potentially attractive alternative catalyst supports because of their high surface area, combined with high macro-porosity (up to 2 cc/g) and low tortousity[1]. The main problem is encountered when such a fluffy materials is used in conventional catalytic reactors. The goal of this work is to investigate how CNFs can be immobilized to macro-structured materials. Two macro-structured materials is used as examples in this work, i.e. ceramic monolith and metal foam. From the perspective of the use of monoliths as structured materials to support catalysts, this work aims on the preparation of improved washcoats based on CNFs, competing the well known relatively dense inorganic washcoats. Metal foams are much less explored as structured catalyst supports and in this case the preparation of stable and uniform washcoats is still a challenge[2].

Experimental

Materials. Ceramic cordierite monolith samples (600 cells per square inch, obtained from Degussa), bare (without washcoat), and with 17 μm average thickness of γ-alumina washcoat, were used. Nickel was deposited on the monolith from a pH-neutral nickel solution (0.1 M).

Ni foam (obtained from RECEMAT) is a three dimensional network of connected strands. Each strand is shaped like a prism. The average characteristic strand width was 80 ± 5 μm and the pore diameter was 0.4 mm.

CNFs formation. The samples were reduced. Then, CNFs were formed catalytically by decomposition of CH_4 or C_2H_4 in the case of monolith, while only C_2H_4 was used to synthesize CNFs on the Ni foams. The conversion of the hydrocarbon used to synthesize the CNFs was determined by on-line chromatographic analysis (Varian GC model 3700 equipped with a 15 m Q-Plot column).

Characterization. The BET surface area, pore volume and pore size distribution were measured by N_2 adsorption-desorption at 77 K using ASAP 2400 (Micromeritics) instrument. The morphology of both CNF and the support structure were studied with Scanning Electron Microscopy (SEM) (LEO 1550 FEG SEM) equipped with EDX analysis. The stability of the CNFs formed on Ni foam towards shear forces, which would be necessary when applied as catalyst support in liquid phase, was tested by flowing water through the foam at room temperature with a linear velocity of 1 m/s. The extent of loss of CNFs was calculated from the difference between the initial and final weight of the foam.

Results and Discussion

Detailed microscopic evaluation of the **monolith** revealed that at the outer surface of the washcoat a hairy layer is formed with a typical thickness of 1 μm containing CNFs exclusively (**micrograph 1.A**). The structure of this layer is similar to the inverse structure of a traditional alumina washcoat, although much thinner. The hairy layer is supported on a composite layer containing both CNF and fragments of the alumina washcoat. The influence of the Ni particle size and synthesis conditions on the properties of the resulting material will be presented. It turns out that the thickness of the CNF layer at the outermost surface as well as the diameter of the fibers increases with mean Ni-particle size.

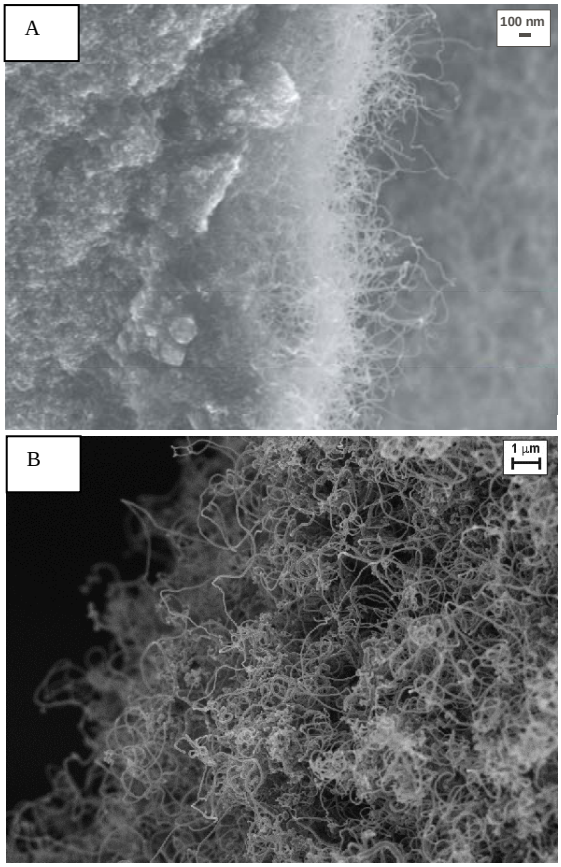

Figure 1. Scanning Electron Micrographs of the CNF layer at the outer surface of (a) monolith loaded with 1.2 wt% Ni. Formation conditions: 200ml/min 50 % CH_4, 10 % H_2 in N_2 at 843 K for 3 hrs (b) Ni foam. Formation conditions: 107ml/min 25 % C_2H_4 in N_2 at 623 K for 3 hrs.

Growing CNFs on the monolith using methane leads to immediate fragmentation and doubling of the thickness of the washcoat independent on the amount of CNFs, forming a macro-porous composite layer of entangled alumina particles and CNF with a typical diameter of 10-30 nm. Immediate fragmentation is due to the fact that some of the fibers are too thick for the pores in the washcoat. The total porosity decreases with the amount of CNF whereas the surface area per gram monolith increases[3].

Large Ni particles are able to grow CNF for longer times, resulting in detachment of the washcoat from the cordierite, which is

caused by extensive growth of CNF out of the washcoat. Furthermore, extended growth of CNF inside the cordierite body causes disintegration of the monolith body when macro-pores are locally overfilled with CNF. Methane is preferred over ethene for growing CNF because ethene grows CNF rapidly even on relatively large Ni particles, resulting in thick fibers up to 70 nm in the macro-porous cordierite, destroying the monolith.

A rough and hairy layer of entangled CNFs (**micrograph 1.b**) was formed on the surface of the **nickel foam**. The surface area of the Ni foam increased from less than 1 m^2/g to about 30 m^2/g. The pore volume of the synthesized CNFs layer is 1 cm^3/g. Moreover, the voids between the CNFs are macropores and thus significantly larger than the typical mesopores in conventional inorganic catalyst supports.

The initial morphology of the surface of the Ni foam was typical for polycrystalline Ni, with grains in the size range between 1 and 10 μm. A rough surface with small Ni particles, sized in the range of 10-100 nm, formed when the polycrystalline Ni surface was exposed to ethene at 450°C for 0.5 hour. Some of the Ni particles started to synthesize CNFs with diameters between 10 and 70 nm. The size of the Ni particles is significantly smaller than the size of the grains in the Ni foam. Thus, fragmentation of the Ni grains into small Ni particles occurs before CNFs start to form. Fragmentation of polycrystalline Ni into small Ni particles is well known in corrosion literature as metal dusting[3].

Figure 2 shows that the formation rate of CNFs on pre-shaped small Ni particles supported on monolith takes off with a high rate followed by deactivation exclusively. In contrast, formation rate of CNFs on polycrystalline Ni foam at constant temperature initially increased, reached a maximum value and then decreased. The initial increase in the formation rate of CNFs on polycrystalline Ni is caused by the necessity of fragmentation of Ni grains into small Ni particles.

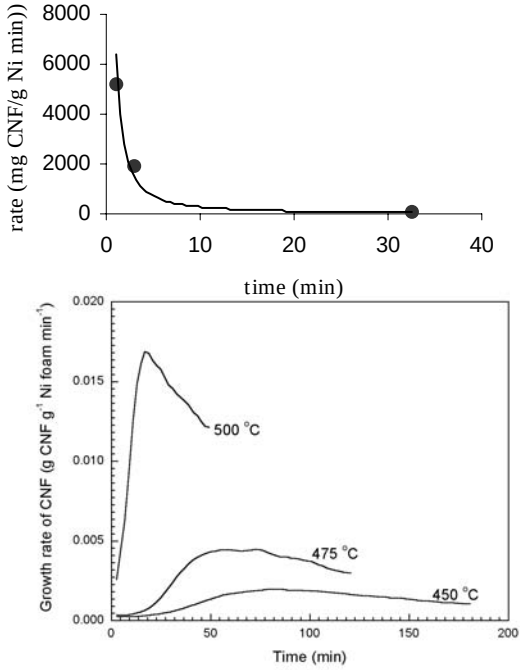

Figure 2. CNFs formation rate on (a) monolith loaded with 3.0 wt% Ni. Formation conditions: 200ml/min 50 % C_2H_4, 10 % H_2 in N_2 at 843 K (b) Ni foam. Formation conditions: 107ml/min 25 % C_2H_4 in N_2.

The integrity of the samples and strong attachment of the CNFs to the Ni surface or to monolith are necessary for application of the final composite materials as structured catalyst supports.

The monoliths can easily disintegrate when CNF formation is excessive, either in the cordierite or on the interface between the cordierite and the washcoat. However, CNFs are always observed in the macro-porous cordierite and it is concluded that the interweaved fiber layer, extending from the cordierite *via* the composite layer to the hairy top layer, is essential to generate mechanical stability of the structure.

The integrity of the Ni foam was lost after synthesizing 138 wt% CNFs at 500°C in 3 hours. On the other hand, the foams were stable after synthesizing 50 wt% CNFs at 450°C in 6 hours. The Ni foam collapsed at high temperature because of the increase in the rate of corrosive metal dusting with temperature[3]**.** The CNF layer on Ni foam can withstand shear forces caused by flowing water (1 m/s) through the foam.

The optimum conditions for generating a macro-porous CNF layer with a high surface area will be presented for both examples, circumventing disintegration of the macro structured materials.

Conclusions

A thin highly porous washcoat based on CNFs on ceramic structures can be synthesized without disintegrating the final composite materials.

Stable Ni-CNFs-foam composite structures can be obtained under the conditions that the extent of corrosive metal dusting of Ni is limited, via decreasing the temperature and/or the formation time. Metal dusting is needed to form small Ni particles that allow formation of CNFs.

Acknowledgement. This work was performed under the auspices of NIOK, the Netherlands Institute of Catalysis Research. The authors gratefully acknowledge Degussa for supplying monolith samples and RECEMAT for supplying Ni foams.

References

(1) De Jong, K., Geus, J., *Catal. Rev. – Sci. Eng.*, **2000**, 42(4), 481
(2) Matatov-Meytal, Y., Sheintuch, M., Applied Catalysis A: General, **2002**, 231,1.
(3) Jarrah, N. A. , van Ommen, J. G., Lefferts, L., J. Mat. Chem.,
(4) Pippel, E., Woltersdorf, J., Schneider, R., Materials and Corrosion, **1998**, 49, 309.

Chemical Processing of bundled Carbon Nanotubes into Macromolecules in Solution

[1]U.J.Kim, [3]C.A.Furtado, [1]X.Liu, [4]R.Saito, [5,6]M.Dresselhaus, [1,2]P.C.Eklund

The Pennsylvania State University, University Park, PA, 16802
[1]Department of Physics,
[2]Department of Materials Science and Engineering,
[3]Centro de Desenvolvimento da Tecnologia Nuclear – CDTN/CNEN, Belo Horizonte, MG, Brazil
[4]Department of Physics, Tohoku University and CREST JST, Sendai 980-8578, Japan
Massachusetts Institute of Technology, Cambridge, Massachusetts 02139-4307, USA
[5]Department of Physics
[6]Department of Electrical Engineering and Computer Science,

Introduction

An effective chemical process to obtain clean, individual single-walled carbon nanotubes (SWNTs) in a stable solution is an important step needed for developing many large scale applications for these molecular filaments, e.g., as electrostatic shielding additives, field emission flat panel displays, radar paints, conductive inks, or in nanotube-polymer composites. Of particular interest, is the potential for chemical change, or damages to the SWNTs during purification. Raman and IR have been found very useful in studying these changes. However, to our knowledge, nobody has used these 2 tools together to chart the outcome of the processing and, in particular, the impact of the processing on the eventual dispersion of individual nanotubes in amide solutions. During the course of this research, we have been able to identify, for the first time, the IR-active modes for small diameter 1.2 -1.6 nm nanotubes.

Experimental

Arc discharge nanotube soot (Carbolex, Inc.; USA) produced using ~4 atomic % Ni-Y loaded carbon electrodes was studied here. To primarily remove amorphous carbon, we either used dry oxidation (DO) or hydrogen peroxide (H_2O_2) reflux. DO involves a thermal soak at 355ºC for 20 minutes in flowing dry air (100sccm). This achieves selective oxidation of the amorphous carbon, and also minimizes nanotube mass loss. Amorphous carbon was also removed by a reflux in 30 vol.% of H_2O_2 in H_2O for 18hrs. The Ni-Y was dissolved by reflux in either 3N HNO_3(16h), or in weakly oxidizing 6N HCl (24h).

The tubes were then "debundled" in N-methyl pyrrolidone (NMP) or N, N-dimethylformamide (DMF) using ultrasound for 4hrs. Centrifugation (14000rpm, 90min) was carried out to remove remaining large bundles or particles. A drop of this solution was placed on a mica substrate and the solvent was evaporated in air and then AFM (Digital Instruments Nanoscope (Model IIIA)) measurements were made to determine the fraction of tubes appearing as single isolated tubes on the substrate.

FTIR and Raman spectra of the raw and processed SWNT samples were collected using a BOMEM DA3+ FT spectrometer that is equipped with. Nd:YAG laser (1064nm).

Results and Discussion

Fig.1 shows Raman spectra collected at various stages of the chemical processing indicated. Above 1000cm^{-1}, two Raman bands are observable; (1) a relatively broad, disorder-induced or "D-band" at ~1350 cm^{-1}, and (2) a first-order-allowed band with substructure appears at1590cm^{-1} (SWNT-G-band). D band intensity and G band width are considered as probes of SWNT wall integrity that may be compromised by chemical processing leading to defect sites or functionalization. The G band has 5 Lorentzian components. We find that only the H_2O_2 and HNO_3 treated samples exhibit broadening of the G band. A small upshift of the peaks is also seen. This sample processing leads to exhibit D band enhancement as well. We also have considered dry oxidation (DO) to remove amorphous carbon and a subsequent HCl reflux to remove catalyst residue. This processing produces no broadening of the G band components. After annealing the DO/HNO_3 sample at 1100ºC for 24h hours in vacuum (Fig.1(g)), the broadened and distorted Raman band returns to that of raw soot, which means the wall damage or functionalization is largely removed. After high T vac annealing the DO/HCl processed soot, no change in the Raman bands was observed.

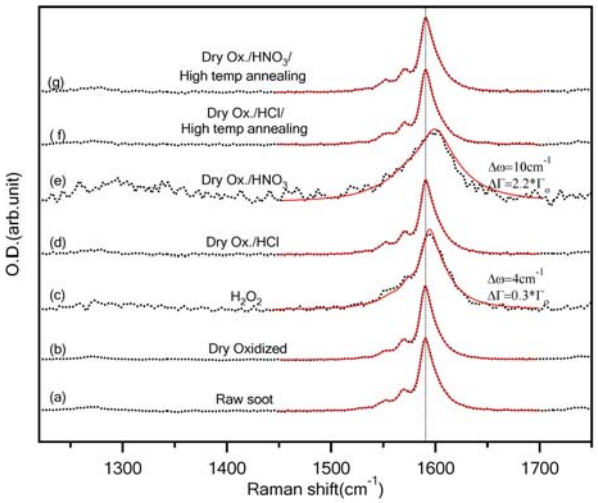

Figure 1. Raman spectra of raw soot (a), DO at 355ºC for 20nm (b), H_2O_2 reflux for 18h (c), DO/HCl (24h) (d), DO/HNO_3(16h) (e), DO/HCl(24h)/annealing at 1100ºC for 24h (f), and DO/HNO_3(16h)/ annealing at 1100ºC for 24h(g).

We have also carried out an FTIR study of the chemically processed SWNT samples. This probe is more sensitive than Raman to functional groups on the tubes. The IR spectra for tubes processed in various ways is shown in Fig.2. The shaded bands in the figure indicate the range where the indicated functional group would appear. As can be seen in Fig.2(a),(b),(d), the IR spectra of DO/HCl is similar to that of the raw soot ,except for an enhancement of the ~1100cm^{-1} band. As seen in Fig.2(c),(e), the band at ~1740cm^{-1}(in the region of C=O stretching vibration) is enhanced in the H_2O_2 and HNO_3 refluxed samples. Note that a very broad band appears in the ~3230-3500cm^{-1} range, (–OH stretching mode) that is consistent with carboxylic acid or hydroxyl functional groups. A new broad band at ~1230cm^{-1} appears which can be assigned as the -OH bending mode. Fig.2(f),(g) show the IR spectra of annealed DO/HCl and DO/HNO_3 at 1100ºC for 24h. By annealing DO/ HNO_3 sample, the broad bands at ~3230cm^{-1} and ~1230cm^{-1} are removed. They appear to be due to –OH. According to Kinoshita, oxygen containing surface groups will be completely eliminated, and –CH groups should be removed, or at least decreased drastically at our annealing conditions[2]. The 3 sharp bands near ~2900cm^{-1} and the bands at ~1380cm^{-1} and 1460cm^{-1} have been assigned previously to –CH asymmetric and symmetric stretching modes and bending modes, respectively by other groups[3]. But as seen in Fig.4, these bands do not decrease in intensity upon annealing. This suggests that they are SWNT phonons. Via connection with theoretical calculations, we can identify most of the sharp vibrational features in the FTIR spectra of high-T annealed samples with SWNT vibrational modes.

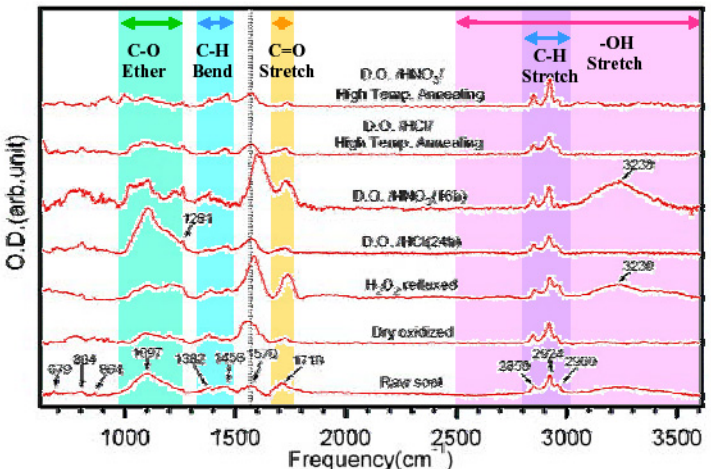

Figure 2. IR spectra of raw soot (a), DO at 355°C for 20nm (b), H_2O_2 reflux for 18h (c), DO/HCl (24h) (d), DO/HNO_3(16h) (e), DO/HCl(24h)/annealing at 1100°C for 24h (f), DO/HNO_3(16h)/ annealing at 1100°C for 24h(g). A smoothly varying electronic background has been subtracted from the data.

Fig. 3(a) is a typical topographic AFM image of ultrasonically processed carbon nanotubes deposited from DMF or NMP solution onto cleaved mica substrates, Fig. 3(b) shows Z scan analysis of the lines labeled as (1), (2), (3), (4) in Fig. 3(a). In Fig. 3(b), the data for lines. (1), (2), (3) all refer to the same tube. The average filament diameter in this case is $\bar{d}$ =1.45nm ± 0.07nm. The line labeled as (4) in Fig. 3(a) cuts across 7 tubes and 2 small particles and the Z scan is also shown in Fig. 3 (b); examples of isolated tubes and very small bundles (2~3 tubes/ one bundle) can be seen.

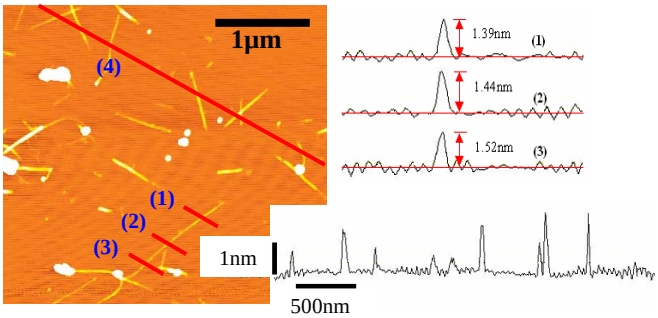

Figure 3. (A) Typical AFM images showing the dispersion of SWNTs in DMFor NMP, (b) shows Z scan analysis of the lines labeled (1),(2),(3),(4) in (a).

To see the real effects of various chemical process schemes on the nanotube dispersion, we show (Fig.4) AFM result for filament height (left) and filament length (right) distributions for several purification/de-bundling processes. For the diameter, DO/HCl/NMP(Fig.4(a)) and H_2O_2/HCl/NMP processing (Fig.4(c)) exhibit a peak in the bin (1.4-2.0nm), consistent with the average diameter (~1.4nm) reported for Carbolex tubes. Interestingly, the AFM data in Fig.4(b) indicates that small diameter tubes are more commonly found after the HNO_3/DMF process than after the HCl/DMF, HCl/NMP or H_2O_2/HCl/NMP processes. The reason for this is not clear; it may be that an HNO_3-reflux preferentially functionalizes smaller diameter SWNTs, causing bundles containing them to be preferentially exfoliated. As observed in Fig,2(e), HNO_3 refluxed sample were functionalized by carboxylic acid and hydroxyl group.

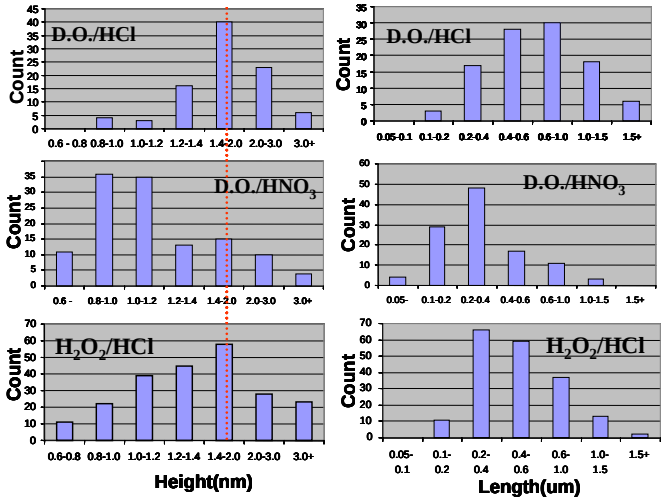

Figure 4. AFM Diameter (left) and length (right) distributions for arc-derived SWNTs after various purification and de-bundling processes.

We can define a quantitative measure of the success in debundling or dispersion by a "dispersion yield"(Y_D), defined as the fraction of the nanotubes found in the final solution as individual nanotubes. From data in Fig's 4(a)-(c) we find Y_D~50% for HCl/(DMF or NMP), Y_D~90% for HNO_3/DMF and Y_D~70% for H_2O_2/HCl/NMP. It is interesting that functionalized tubes by HNO_3 reflux or H_2O_2 reflux produce better dispersion yield in amid solvents. In one experiment, to investigate the effects of HNO_3 reflux on debundling, we then tried to disperse the bundled SWNT material in amides (DMF and NMP) after annealing HNO_3 refluxed SWNTs at 1100°C under vacuum (10^{-7} Torr). We found that the purified and high-T annealed material dispersed much less efficiently. This may be evidence that functional groups aid the debundling process in amid solvents. In Fig.4((d)-(f)) we exhibit the length distributions for the debundled tubes obtained from AFM z-scan analysis whose diameter distributions appear in Fig.4((a)-(c)). HNO_3-and HCl reflux were found to reduce the average tube length to ~300nm and ~800nm, respectively, whereas the H_2O_2/HCl/NMP(Fig.4(f)) exhibits shorter tube length(~500nm) than DO/HCl/NMP; H_2O_2 may cut the tubes, as proposed earlier.

Acknowledgement. This work was supported by NSF-DMR-0103585, and NSF-DMR-0304178 and the PSU MRSEC-DMR-0213623. C. A. Furtado thanks CNPq-Brazil for financial support.

References

[1] C. A. Furtado, U. J. Kim, H. R. Gutierrez, Ling Pan, E.C. Dickey, and Peter C. Eklund, accepted in J.Am.Chem.Soc in March,2004

[2] Kinoshita, K. In Carbon - Electrochemical and Pysicochemical Properties; John Wiley & Sons, Inc., Ed.; New York, 1988;Chapter 3.

[3] Bishun N. Khare, M. Meyyappan, Alan M. Cassell, Cattien V. Nguyen, and Jie Han, Nano Lett., V2, 2002, 73

CARBON NANOTUBES AS A CHEMICAL SENSOR

G. U. Sumanasekera[1], B. K. Pradhan[2], C. K. W. Adu[3], R. E. Romero[3], P. C. Eklund[3].

[1]Department of Physics, University of Louisville, KY 40292
[2]Columbian Chemicals Company, Marietta, GA 30062
[3]Department of Physics, Penn State University, University Park, PA 16802

Introduction

Carbon nanotubes have extremely interesting and unique chemical and physical properties. These properties are being investigated for vital applications such as field emission devices, actuators, nano-electronics, gas storage, etc.[1]. These application can involve individual nanotubes, individual bundle of nanotubes, or mats of entangled bundles of nanotubes. Recent reports show the capability of carbon nanotubes as chemical sensors. It has been demonstrated experimentally that very small concentrations of gas molecules (NO_2 and NH_3) can substantially change the electrical transconductance of individual field-effect transistors based on *semiconducting* nanotubes, and this property can be used for the design of high sensitivity chemical sensors[2]. In these cases, charge transfer is suspected to amplify the effect of adsorption. Other experimental investigations have shown that O_2 adsorption has a significant effect on the electrical transport of carbon nanotubes and induces a change in sign of the TEP [3–4]. Charge transfer [5] and the presence of defects [6,7] have been identified as important to the O_2–SWNT system. Interestingly, small systematic changes in the resistivity and the TEP of SWNTs were also observed due to collisions with non-reactive gases[8] and small molecules (He, Ne, Ar, Ne, Kr, Xe, N_2, CH_4, and H_2). In such cases, the changes in *S* and *R* upon gas exposure were identified as resulting from weak interactions between the gas and the metallic nanotubes that induce changes in the electron and hole free carrier lifetimes. These results also suggested that even gas collisions with the nanotube walls at a few hundred degrees celsius and 1 atm affect the transport properties of SWNTs]. In this paper, we present the results of a systematic study of the changes in the TEP and four-probe resistance of vacuum-degassed thin films of nanotube bundles induced by the adsorption of (a) polar alcohols ($C_nH_{2n+1}OH$; n = 1–4) and water (b) six-membered ring molecules (C_6H_{2n}; n = 3–6)]. Someya *et al* [9] have reported on the influence of alcohols on the characteristics of field-effect transistors (FET) fabricated from individual carbon nanotubes. They observed significant, reversible changes in the FET drain current when the device is exposed to various kinds of alcoholic vapors.

Experimental

The SWNT material studied here was obtained from CarboLex, Inc., and consisted of ~50-70 vol% carbon as SWNTs produced by the arc discharge method using a Ni–Y catalyst. Chemical purification of the arc-derived material was carried out in a two-step process: (1) oxidation in dry air for 30 min at 350 ^{0}C followed by (2) refluxing in 4 M HCl at
120 ^{0}C for 4 h. The purified SWNT material was then finally subjected to a ~10^{-7} Torr vacuum-degassing process at 1000 ^{0}C for 24 h. SWNT samples were in the form of thin films
of tangled ropes deposited from an ethanol suspension onto a glass substrate. Two chromel–Au/7 at.% Fe thermocouples and two additional Cu leads were attached with small amounts of silver epoxy to four corners of the 2 mm× 2 mm sample to measure the TEP and the DC four-probe electrical resistance simultaneously. The TEP (i.e., Seebeck coefficient) data were collected using a heat pulse technique[9]. The nanotube sample was also vacuum-degassed *in situ* in the TEP apparatus at 500 K before water or various $C_nH_{2n+1}OH$ molecular vapors were introduced. A glass bulb containing the water or alcohol or hydrocarbon liquids was connected via a valve to the TEP apparatus. All the chemicals were spectral grade (Sigma-Aldrich, Co.) and had been previously vacuum-degassed. After the thermoelectric and resistive responses to a particular molecular vapor were recorded, the sample was then degassed *in situ* at 500 K again until the TEP and four-probe resistance of the sample returned to the original 'degassed' values. Then the same film was exposed to the next molecular vapor and so on.

Results and Discussion

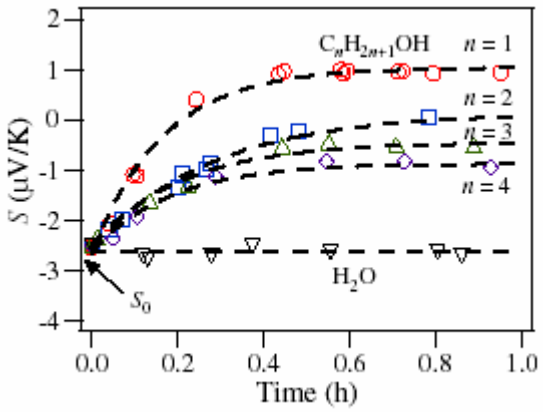

Figure 1. The time dependence of the TEP response of a SWNT thin film to successive exposure to vapours of water and alcohol molecules ($C_nH_{2n+1}OH$; n = 1–4) at 40 ^{0}C. Dashed curves are fits to *S(t)* data using an exponential function.

In Fig. 1 we show the *in situ* thermopower response to the vapors of alcohols and water. It is seen that for methanol, ethanol, isopropanol and butanol the TEP also rises exponentially with time from the degassed value S_0 ~ -2.7 μV/K to a higher plateau after ~1 h. For methanol and ethanol, *S* is even driven positive, saturating at S_{max} ~ +1.1 and +0.1 μV/K, respectively. Exposure to larger alcohol molecules, i.e., isopropanol and butanol, is found to lead to smaller changes in *S* and saturation at S_{max} ~ -0.5 and -1.0 μV/K, respectively. Interestingly, exposure to water vapour (another small, but very polar molecule) induces virtually no change in the TEP. Bradley *et al* [8] have also found very weak or no response of the TEP of mats of bundled SWNTs to water vapour. Concomitantly, exposure to methanol shows the largest change in the four-probe resistance *R*, with an increase of ~8.2%. The exposure to methanol, ethanol, isopropanol, butanol and water induce an increase in R, with $\Delta R/R$ saturating at ~8.2%, 7.5%, 6.8%, 5.4% and 4.4%, respectively. Both *R(t)* and *S(t)* exhibit simple exponential behavior.

Figure 2 displays the evolution of the thermopower versus the fractional change in the four-probe resistance ($\Delta R/R_0$) at fixed temperature (40 ^{0}C). As the coverage of the molecules on the SWNTs increases with increasing time of exposure to the respective molecular vapour, both *S* and $\Delta R/R_0$ increase. It is very important to note that the data for all the alcohols show linear behaviour for *S* versus $\Delta R/R_0$, consistent with physisorption and not for a chemisorption process involving significant charge transfer. Thus, the linearity of *S* versus $\Delta R/R_0$ implies that little or no charge transfer is taking place between the adsorbedmolecules and the SWNTs; i.e.,

H_2O and the alcohols that are physisorbed onto high *T* annealed films do not chemically dope the SWNTs.

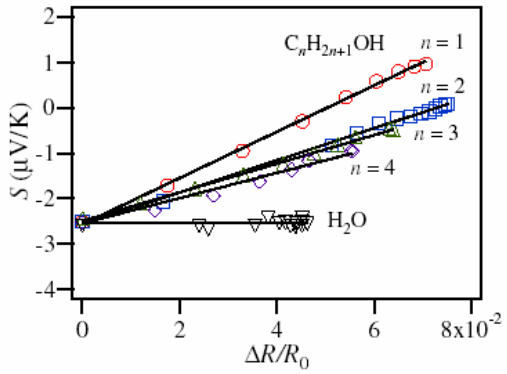

Figure 2. *S* versus $\Delta R/R_0$ plots during exposure of degassed SWNT bundles to water and $C_nH_{2n+1}OH$; *n* = 1–4. The solid lines are linear fits to the data until saturation is established.

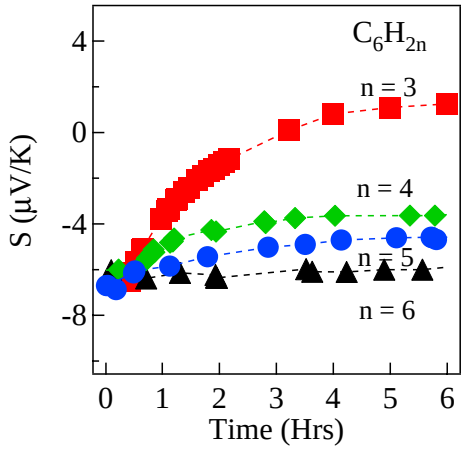

Figure 3. In situ 40 ^{0}C thermoelectric power (S) vs time (t) during successive exposure of a degassed SWNT film to vapors of six-membered ring molecules C_6H_{2n}; n = 3–6. The dashed lines are guides to the eye.

In Fig. 3 we show the *in situ* thermopower response with time to the vapors of benzene (C_6H_6), 1,3-cyclohexadiene (C_6H_8), cyclohexene (C_6H_{10}), cyclohexane (C_6H_{12}). For C_6H_6 (benzene), with increasing exposure time, the thermopower is seen to increase with time from its initial (degassed) value *S* = -6.4 μV/K, eventually saturating after ~6 h at a positive value *S* = +1.3 μV/K. Subsequent exposure to 1,3- cyclohexadiene leads to a similar time dependence of the thermopower and a saturation at ~3.6 μV/K. Cyclohexene was studied and found to induce a smaller change in thermopower, saturating at *S*=4.6 μV/K. Interestingly, cyclohexane, which has no π electrons, was found to exhibit no detectable change in the thermopower. Concomitantly, exposure to benzene shows the largest change in resistance with an increase of 13% at saturation. 1,3-Cyclohexadiene and cyclohexene induce increases in resistance saturating at 10% and 7%, respectively. Consistent with the thermopower results, exposure to cyclohexane shows essentially no change in four-probe resistance. Fig. 4 shows the S vs $\Delta R/R_0$ for each C_6H_{2n}; n = 3–6. As shown in Fig. 4, a universal behavior (i.e., independent of *n*) is observed for the dependence of the thermopower on the change in resistance $\Delta R/R_0$. This non-linear character in the C_6H_{2n}/SWNT system is not well understood, and we have tentatively identified it with a multiple-electron-scattering process].

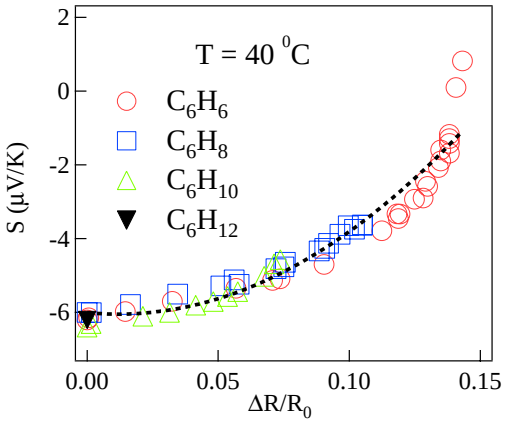

Figure 4. *S* vs $\Delta R/R_0$ during exposure to C_6H_{2n}; n = 3–6. The dashed curve is a fit of a quadratic function

Conclusions

We have utilized *in situ* measurements of TEP and resistivity to investigate the adsorption of various hydrocarbons with varying number of π electrons, polar molecules (alcohols and water) in bundled SWNTs. We observe a strong effect on both the TEP and resistivity for methanol, ethanol, isopropanol and utanol.Surprisingly, water vapour does not have any effect on the TEP. We have also observed that *S* exhibits a linear relationship with $\Delta R/R_0$, consistent with the creation of a new impurity scattering channel via physisorption. We observe strong, systematic effects on the resistance and thermopower for six-membered ring hydrocarbons and a universal behavior is observed for *S* vs $\Delta R/R_0$.

References

(1) Dresselhaus, M. S; Dresselhaus, G; Eklund; P. C., 1996 *Science of Fullerenes and Carbon Nanotubes* (San Diego, CA: Academic)

(2) Kong; J., Franklin; N. R., Zhou; C., Chapline; M. G., Peng; S., Cho; K ., Dai; H., **2000** *Science, 287* 622

(3) Collins, P. G.; Bradley, K.; Ishigami, M.; Zettl, A., *Science*, **2000**, *287*, 1801

(4) Sumanasekera, G. U.; Adu, C. K. W.; Fang, S. L.; Eklund, P. C., *Phys. Rev. Lett.*, **2000**, *85*, 1096

(5) Jhi, S-H; Louie, S. G.; Cohen, M. L., *Phys. Rev. Lett*, **2000**, *85*, 1710

(6) Ulbricht H.; Moos, G.; and Hertelet al, *Phys. Rev. B*, **2002**, *66*, 075404 (2002)

(7) Goldoni; A., Larciprete; R., Petaccia; L., Lizzit; S., **2003** *J. Am. Chem. Soc. 125* 11329

(8) Adu, C. K. W.; Sumanasekera, G. U.; Pradhan, B. K.; Romero, H. E.; Eklund, P. C., *Chem. Phys. Lett.*, **2001**, *337*, 31

(9) Someya; T., Small; J., Kim; P., Nuckoll; C., Yardley; J. C., **2003** *Nano Lett. 3* 877

(10) Sumanasekera, G. U.; Grigorian, L.; Eklund, P.C., Meas. Sci. Technol., **2000**, *11*, 273

CARBON NANOTUBE NANOELECTRONIC DEVICES FOR CHEMICAL DETECTION IN LIQUID HYDROCARBONS

Alexander Star, Keith Bradley, Jean-Christophe P. Gabriel and George Grüner

Nanomix Inc.
5980 Horton Street, Suite 600.
Emeryville, CA 94608

Introduction

Hydrocarbon fuels are complex mixtures of 150-260+ aliphatic and aromatic hydrocarbon compounds containing varying concentrations of benzene, n-hexane, toluene, xylenes, naphthalene, and certain n-C9-C12 fractions.[1] Due to their natural petroleum base, the chemical composition of different hydrocarbon fuels is not defined, and the fuels are classified according to broad performance criteria such as flash and boiling points, complicating chemical comparisons. The recent emergence of nano-scale electronic devices offers the opportunity for extremely sensitive detection of chemicals by monitoring the device characteristic when the devices or their components are exposed to an environment where the chemicals are present.

In this work, we have used field-effect transistors fabricated using semiconducting carbon nanotubes (NTFETs).[2] Such devices have been recently explored as chemical sensors.[3,4] The response of the device characteristics to chemical analytes in the gas phase occurs through charge transfer between the nanotube conducting channel and the analytes, as evidenced by experiments involving electron donating (NH_3) and electron withdrawing (NO_2) molecules.[4]

Experimental

NTFET Devices. NTFET and NTNFET devices were prepared according to published procedures,[5] using standard photolithography techniques on 100 mm wafers. NTFET devices were fabricated using SWNTs grown by chemical vapor deposition (CVD) at 900°C using dispersed iron nanoparticles as growth promoter and a methane/hydrogen gas mixture. Electrical leads were patterned on top of the nanotubes from titanium films 30 nm thick capped with a gold layer 120 nm thick. A fair proportion of the tens of thousands of devices made on each wafer are p-type NTFET with a modulation of 1 (tested using an autoprober), indicative that for those devices only semiconducting nanotubes are present. The devices used in this study were selected among those.

Electronic Measurements. Electronic measurements of NTFET devices, such as current flow between S/D electrodes as a function of applied gate voltage, were conducted using a semiconductor parameter analyzer (Keithley 4200). Devices in air were contacted with pin probes. A glass pipette was used to position a drop of liquid on the device. Chemicals were purchased from Aldrich and used as received.

Results and Discussion

Figure 1 depicts the schematic layout of the NTFET device architecture. SWNTs on silicon substrates contacted with metal (Ti / Au) contacts, together with a doped Si back gate, form the basic elements of the NTFET. In the actual devices, multiple nanotubes were connecting the source and drain electrodes. We have monitored the change of the source-drain current (I) as a function of the gate voltage (Vg) both with increasing and decreasing gate voltages. In devices that have a multitude of nanotubes, both metallic and semiconducting nanotubes contribute to the source-drain current. For the experiments reported here, devices dominated by semiconducting nanotube transistor channels were selected using a wafer autoprober.

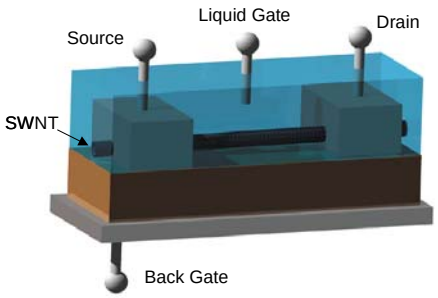

Figure 1. Detection in liquids with NTFET devices by using either back gate or liquid gate configurations.

As expected, the conductivity of the liquids plays an important role in NTFET device operation using a silicon back gate. With conductive liquids, such as water, (i) the screening of the gate voltage prevents gating of the device, (ii) the liquid provides an additional conduction channel, and (iii) mobile ions associated with the conducting liquid lead to a large hysteresis. On the other hand, in liquids with low conductivity such as cyclohexane and toluene, the device conductance is dominated by the nanotube channel and the operation of NTFET changes little as compared to air.

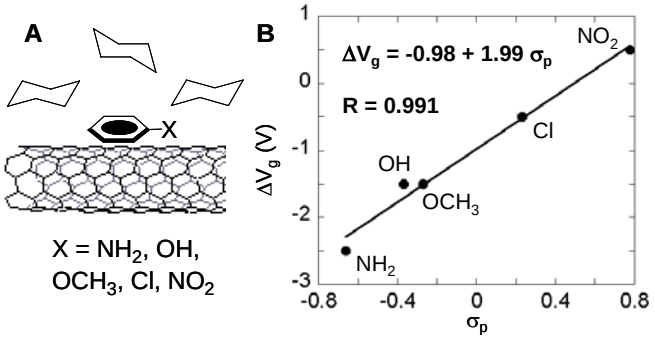

Figure 2. Detection of aromatic compounds with NTFET devices. (A) Schematic of a single wall carbon nanotube conducting channel with a monosubstituted benzene molecule adsorbed on the side-wall of the nanotube in a cyclohexane solution. (B) Linear regression analysis of the gate voltage shift (ΔV_g) of devices in 0.1M cyclohexane solutions of the selected aromatic compounds.

We have explored[6] the effects of monosubstituted benzene compounds, such as aniline, phenol, anisole, toluene, chlorobenzene, and nitrobenzene, on the NTFET device characteristic (**Figure 2**). The compounds all have similar geometry in their non-covalent binding to the carbon nanotube conducting channel, but substituent groups on the benzene ring provide different inductive and resonance effects upon binding. Consequently their relative electron donating effects (NH_2>OH>OCH_3>Cl>NO_2) are well known. The charge transfer to the nanotube channel can be estimated from the empirical Hammett constants (σ_p) of the substituents on these aromatic compounds. A clear linear relation with a positive slope (ρ value) of +1.99 is found between the gate voltage shift and the Hammett values (**Figure 2B**).[6]

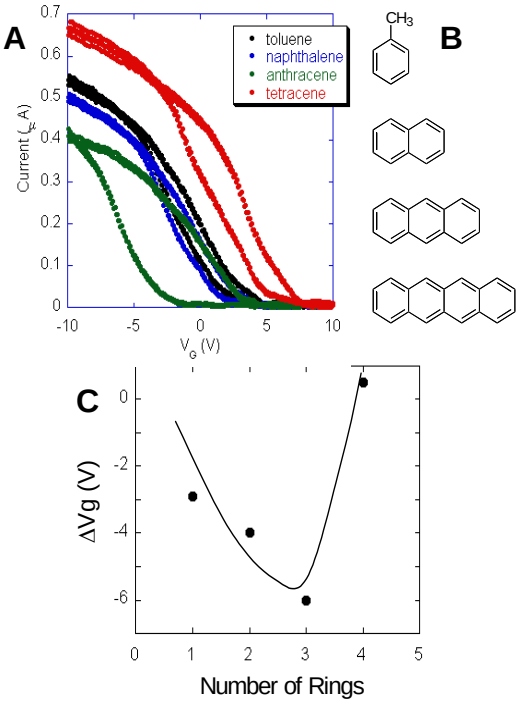

Figure 3. Comparison of number of aromatic rings with the NTFET response, i.e. I-Vg dependence. (A) The response to 0.5 mM solutions of naphthalene, anthracene, and tetracene in toluene, as compared to pure toluene solvent. (B) Chemical structures of the aromatic compounds. (C) Threshold gate voltage shift as a function of the number of aromatic rings in the studied compounds. Threshold shift (ΔVg) is calculated as a shift of the device characteristics in air.

We have also explored the effect of a number of aromatic rings on the NTFET device characteristics. Source-drain current dependence on the gate voltage, I-Vg, shows significant shift in threshold values when larger aromatic compounds, such as naphthalene, anthracene, and tetracene were added to toluene. (**Figure 3A)** The value and the direction of the threshold shift is characteristic for each aromatic compound. While the binding energy of aromatic compounds increases with the number of rings, the charge transfer to nanotube transistor channel is expected to remain the same per aromatic ring unit. The exposure to toluene solvent (one ring) results in ~3 V threshold shift to more negative gate voltage values, as compare to air. The addition of larger aromatic compounds with two and three rings in toluene results in progressive negative shift. However, the addition of tetracene (four rings) introduce an unexpected positive shifts (**Figure 3C**). The observed change in the response is probably due to curvature of carbon nanotubes. These results imply that NTFET can be potentially used for characterization of aromatic hydrocarbons, not only by their charge transfer to carbon nanotube transistor channel, but also by their geometrical parameters.

In addition to aliphatic and aromatic hydrocarbons, hydrocarbon fuels may contain certain additives, such as amines, alcohols and ethers (MTBE). NTFET devices have been already shown to be sensitive to different alcohols[7] and amines.[8] Here, we have investigated the selectivity of the response to amino compounds of the NTFET device characteristics. The addition of amino compounds into cyclohexane solution result in a significant threshold shift (**Figure 4A**). This threshold shift is analogous to the concentration-dependent shift observed when NTFET devices with liquid gate were exposed to aqueous ammonia.[9] The response to amines is selective as evident from the control experiment, where oleic acid, an organic acid with approximately same number of carbons, was dissolved in cyclohexane (**Figure 4B**).

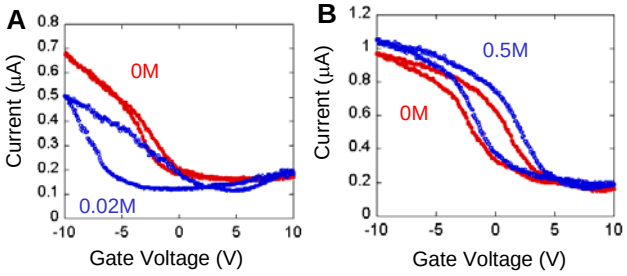

Figure 4. Detection of amino compounds by NTFET. The device characteristics, I-Vg in the presence and absence of the chemical. (A) Response to 0.02 M of 1-hexyldecylamine in cyclohexane. (B) Control experiment with 0.5 M of oleic acid in cyclohexane.

Conclusions

We have shown that NTFETs can be used for selective detection of aromatic hydrocarbons and amino compounds in the presence of aliphatic / aromatic hydrocarbons. Potentially, NTFET devices can be used as small low power electronic probes to monitor hydrocarbon fuel composition, including amine and ethanol fuel additives both in vapor and liquid phases.

Acknowledgment. We acknowledge the Nanomix technical staff for their assistance with device fabrication and measurements. This work was supported partially by Environmental Protection Agency, under contract EP-D04-045.

References

1. Ritchie, G. D., Still, K. R., Alexander, W. K., Nordholm, A. F., Wilson, C. L., Rossi, J., Mattie, D. R., *J. Toxicol. Env. Health*, **2001**, *4*, 223-312.
2. Tans S., Verschueren A., Dekker C., *Nature* **1998**, *393*, 49–52.
3. Collins P. G., Bradley K., Ishigami M., Zettl A., *Science* **2000**, *287*, 1801–1804.
4. Kong J., Franklin N. R., Zhou C., Chapline M. G., Peng S., Cho K., Dai H., *Science* **2000**, *287*, 622–625.
5. Gabriel, J.-C. P., *Mat. Res. Soc. Symp. Proc.* **2003,** *762*, Q.12.7.1-7.
6. Star, A., Han, T.-R., Gabriel, J.-C. P., Bradley, K., Grüner, G., *Nano Lett.* **2003**, *3*, 1421-1423.
7. Someya, T., Small, J., Kim, P., Nuckolls, C., Yardley, J. T., *Nano Lett.*, **2003**, 3, 877-881.
8. Kong, J., Dai, H., *J. Phys. Chem. B* **2001**, *105*, 2890-2893.
9. Bradley, K., Gabriel, J.-C. P., Briman, M., Star, A., Grüner, G., *Phys. Rev. Lett.* **2003**, *91*, 218301.

KINETICS OF OXYGEN DESORPTION/ADSORPTION IN SWNTs

U. K. Patel, R. Jalilian, S. Desai, J. Rivera, and G.U. Sumanasekera

Department of Physics, University of Louisville, KY 40292

Introduction

Very recently, much attention has been focused on the fundamental science and applications of carbon nanotubes in gas adsorption. Interest on this subject has been heightened by several observations of changes in the electrical conductance of SWNT via gas or chemical adsorption, and a clear interdependence of gas adsorption and transport properties is being established. For example, two research groups[1,2] have reported unusual sensitivity of the electrical resistivity and thermoelectric power (S) of SWNTs to the adsorption of oxygen. They have argued that SWNTs are easily doped with O_2 under ambient conditions, forming a weak charge transfer complex ($C^{+\delta}{}_pO_2{}^{\delta-}$), and adsorbed oxygen changes the sign of the thermopower[3]. Similar results have been observed for multiwall carbon nanotubes and activated carbon fibers. However, this conclusion has been contested *via* FET studies by Avouris and coworkers[4], who find that O_2 dopes the electrical contacts made to the SWNT, and not the wall. In a recent publication, Ulbricht el al.[5], argue that minority oxygen species located either at defect sites on the SWNT bundles or at tube-metal contacts in electronic devices are responsible for the observed p doping. In fact, several mechanisms may explain such phenomena. The gas molecules could affect transport properties indirectly, by binding to donor or acceptor centers in the substrate, or at the contacts, or directly, by binding to the nanotube. In the latter case, the gas could be physisorbed (bound by dispersive van der Waals forces) or chemisorbed (bound by formation of chemical bond resulting some charge transfer), and adsorption could take place either on perfect nanotube walls or at defect sites. Experimentally, a way to distinguish physisorption from chemisorption is to check for a linear relation between the thermoelectric power and the additional resistance induced by gas adsorption[6]. According to this criterion, O_2 is chemisorbed. However, a recent experimental study of the kinetics of oxygen adsorption and desorption on SWNT shows the estimated binding energy is low and consistent with physisorption of oxygen in molecular form. It also remains unclear whether atomic or molecular oxygen is responsible for the charge transfer.

Experimental

The sample used in our study was a commercial bucky paper made of SWNTs grown by laser ablation with an average diameter of 1.4 nm. After purification by refluxing in 2-3 M nitric acid, the tubes have been dissolved in a Sodium Lauryl Sulfate (SLS) surfactant solution. We studied the sample as received (contaminated with surfactant) and after annealing at 1200 ^{0}C at 10^{-7} Torr for 24 hrs to remove the surfactant. Two, Chromel-Au/7at.%Fe thermocouples (all 0.003" dia. wires) were attached to the edges of the sample with small amounts of silver epoxy to measure the thermoelectric power (TEP). The thermopower (*i.e*), Seebeck coefficient data were collected using a heat pulse technique[7]. The sample was placed in an apparatus equipped with a turbo molecular pump capable of evacuating to 10^{-7} Torr for in situ studies which can be heated to 600 K.

Results and Discussion

The thermopower curves during desorption of oxygen for the sample without surfactant at four different temperatures are shown in Fig. 1. The best fits for a double exponential of each graph is also shown in the figure. The fits with a single exponential with the experimental data do not show good agreement and deviate from the experimental data. Whereas, a two exponential function fits the experimental data quite well.

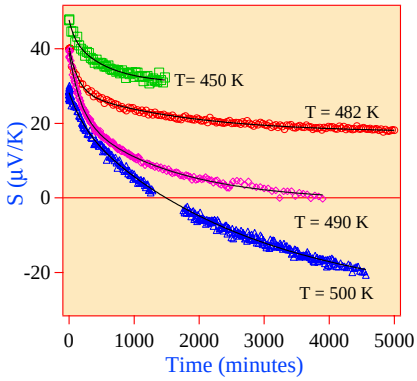

Figure 1. Thermopower versus time at four different temperatures for SWNTs sample free of surfactant during desorption of oxygen. Best fits with two exponentials are shown in solid lines.

The results of oxygen desorption kinetics of the SWNT sample containing surfactant are shown in Fig.2 for two dfferent temperatures. Again the data can be very well fitted with two exponentials.

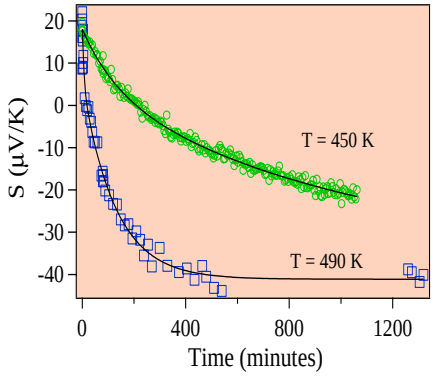

Figure 2. Thermopower versus time at two different temperatures for SWNTs sample contaminated with surfactant during desorption of oxygen. Best fits with two exponentials are shown in solid lines.

These observations show that oxygen has at least two adsorption sites available in SWNT bundles corresponding to the two exponentials. These two sites with different binding energies for oxygen adsorption results in different time constants**.** The comparison of the desorption graphs for the two samples with and without surfactant also reveals that the desorption of oxygen for the SWNTs containing surfactant is faster than that of annealed sample (free of surfactant) at a given temperature. This can be understood as due the wall defects induced on the nanotube walls during the purification process with nitric acid. Due to the presence of wall defects, oxygen can desorb relatively easily compared to the annealed sample. So, in the case of the sample without surfactant, the oxygen is tightly bound to the walls of the tubes compared to the sample with surfactant. Hence, the loosely bound oxygen molecules are relatively easy to be desorbed and result in shorter time for the thermopower to saturate compared to tightly bound oxygen in the case of annealed sample. From above data it is a marked difference that the SWNT free of surfactant with ambient doping with oxygen

has the positive thermopower of about 40 μV/K compared to the one containing surfactant having thermopower of only 20 μV/K. Moreover, in the case of the sample with surfactant, for a given temperature e.g., 490 K the thermopower saturates at a higher negative value of ~ – 40 μV/K compared to the saturated thermopower of ~ -4 μV/K for the annealed sample. This can be explained with the aid of band structure diagram of the SWNTs where in the simplest case, for a fully compensated sample with holes and electrons contributing equally gives zero thermopower for a symmetric band structure[8]. When the sample is doped with the oxygen, which is an acceptor, the Fermi energy moves towards the acceptors states and pinned at these acceptor levels. During the desorption, the Fermi energy E_F is pinned at the donor states presumably introduced by the wall defects. Recently, Larciprete et al.[9], have used photoemission spectroscopy to study the interaction between oxygen and nanotubes. They have found strong interaction of oxygen and nanotubes contaminated with surfactant and interpret the results as due to charge transfer from the nanotube to the Na-O complex. But they find weak interaction of oxygen with nanotubes free of surfactant.

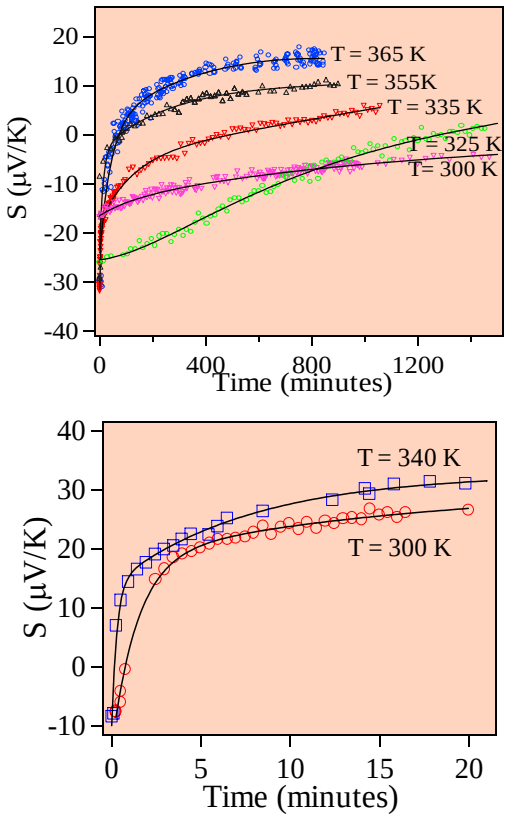

Figure 3. Time evolution of Thermopower during O2 adsorption at various temperatures for (a) SWNTs sample contaminated with surfactant (b) SWNTs free of surfactant. Best fits with two exponentials are shown in solid lines.

The thermopower curves for adsorption of oxygen for the two samples with and without surfactant are shown in Fig. 3 for different temperatures with best fits for two exponentials. The comparison of these two graphs shows that the adsorption of oxygen is faster in the case of the annealed sample compared to the sample contaminated with surfactant. This is due to presence of surfactant obstructing the diffusion of oxygen resulting delays in the adsorption**.**

The time constants extracted from desorption data reflect the strength of the oxygen-nanotube interaction with an activated behavior which requires an extra energy to desorb the oxygen molecule in excess of the binding energy. The temperature dependence of the time constants for the two adsorption sites can be used to estimate the difference between the binding energies of the two sites.

Conclusions

Our study on sensitivity of thermopower of bundles of SWNTs to adsorbed oxygen gas molecules reveal that there are at least two sites available for the adsorption of oxygen in the entangled bundles of nanotubes. The ends of the naotubes are believed to be closed, but wall damages can exist in the tubes. The faster kinetics of the desorption of oxygen in single wall carbon nanotubes contaminated with surfactant compared to the nanotubes free of surfactant is attributed to the wall damages induced by acid treatment during the purification process. The presence of surfactant obstructing the diffusion of oxygen during adsorption result in slower kinetics in the contaminated sample. The magnitude of the thermopower at the saturation for adsorption/desorption is consistent with the band structure analysis. The t emperature dependence of adsorption/desorption time constants allows us to compare the binding energy for the two adsorption processes.

Acknowledgement. This work was supported by funds from Department of Energy (Grant No: DE-FG02-00ER45832). We thank Profs. P. C. Eklund at Pennsylvania State University and S. Y. Wu at University of Louisville for useful discussions.

References

(1) Collins, P. G.; Bradley, K.; Ishigami, M.; Zettl, A., *Science*, **2000**, *287*, 1801
(2) Sumanasekera, G. U.; Adu, C. K. W.; Fang, S. L.; Eklund, P. C., *Phys. Rev. Lett*., **2000**, *85*, 1096
(3) Jhi, S-H; Louie, S. G.; Cohen, M. L., *Phys. Rev. Lett*, **2000**, *85*, 1710
(4) Derycke, V.; Martel, R.; Appenzeller, J.; Avouris, Ph., *Nano Letters*, **2001**, *1*, 9.
(5) Ulbricht H.; Moos, G.; and Hertelet al, *Phys. Rev. B*, **2002**, *66*, 075404 (2002)
(6) Adu, C. K. W.; Sumanasekera, G. U.; Pradhan, B. K.; Romero, H. E.; Eklund, P. C., *Chem. Phys. Lett*., **2001**, *337*, 31
(7) Sumanasekera, G. U.; Grigorian, L.; Eklund, P.C., Meas. Sci. Technol., **2000**, *11*, 273
(8) Romero,H. E.; Sumanasekera, G. U.; Mahan, G. D.; Eklund, P. C., *Phys. Rev. B*. **2000**, *65*, 205410.
(9) R. Larciprete, A. Goldoni, S. Lizzit, Nucl. Instr. and Meth. in Phys. Res. B, **2003**, *200*, 5

APPLICATIONS OF FUNCTIONALIZED SINGLE-WALLED CARBON NANOTUBES

Elena Bekyarova, Bin Zhao, Rahul Sen, Mikhail E. Itkis, Robert C. Haddon

Center for Nanoscale Science and Engineering, Departments of Chemistry and Chemical & Environmental Engineering, University of California, Riverside, California 92521-0403

Introduction

The outstanding materials properties of single-walled carbon nanotubes (SWNTs) have increased the level of interest in their applications. However, many of the potential applications of SWNTs are hindered by the difficulties in their processing. The chemical functionalization of SWNTs will play a key role in the realization of the promise of this material. The solubilization of SWNTs by attachment of long-chain molecules to the open ends of the nanotubes was the first step in brining SWNTs into the realm of molecular chemistry.[1] Rapid progress in development of methods for covalent attachment of various organic groups,[2-6] quantum dots[7] and biological molecules[8] has broadened the opportunities for applications of SWNTs. With the advancement in the chemistry of SWNTs it is now possible to tailor the electronic and chemical properties of SWNTs.[9,10]

Some of the important issues addressed by the chemistry of SWNTs involve dissolution of SWNTs and bundle exfoliation. The chemical functionalization of SWNTs has been shown to increase their solubility in organic solvents and facilitate their processing.[1,11,12] It has also been demonstrated that the chemical functionalization affects the SWNT rope size and results in exfoliation into smaller bundles and individual nanotubes. These issues are especially important for the fabrication of high-performance composite materials, controlled assembling of molecular electronics and development of ultra-high sensitive sensor devises.

Here, we outline chemical approaches to functionalized SWNTs with an emphasis on their application for high-performance composites and biosensors.

Functionalization of SWNTs with oligomers and polymers

SWNTs are considered to be the ideal reinforcing fibers due to their exceptional mechanical, electronic and thermal properties, low density and high aspect ratio. However, the incorporation of SWNTs into the polymer matrix is often problematic due to the chemical inertness of SWNTs. The covalent functionalization of SWNTs is a valuable route towards the development of high-performance composites. It provides homogeneously dispersed SWNTs incorporated in the polymer and a strong interfacial bonding between the polymer and SWNTs. We have applied chemically functionalized SWNTs to prepare a number of SWNT-polymer composite materials.

In one approach, poly (m-aminobenzene sulphonic acid), PABS, a conducting water soluble polymer, was covalently attached to chemically functionalized SWNTs (Scheme 1).

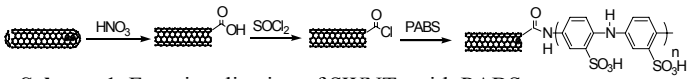

Scheme 1. Functionalization of SWNTs with PABS.

AFM analysis has shown that the PABS-functionalized SWNTs exist in small bundles of 2 to 6 nanotubes (Figure 1). The graft co-polymer (PABS-SWNTs) has high solubility in water (5 mg/ml),[12] which makes the material especially attractive for biological applications. In one study, PABS-funcionalized multi-walled carbon nanotubes have been used as a substrate for neuron growth and have shown an ability to control the neurite outgrowth.[13]

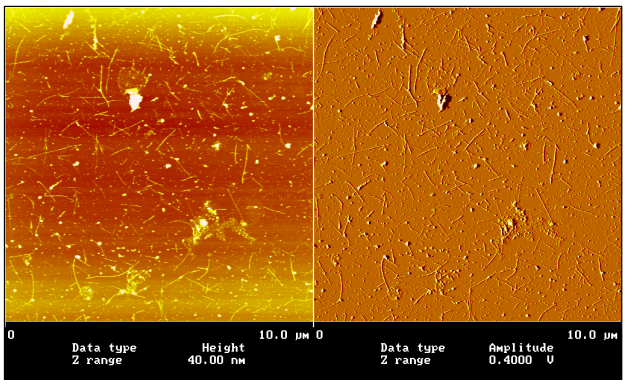

Figure 1. AFM image of SWNT-PABS showing bundles of 4-6 SWNTs.

In another study we have prepared SWNT-reinforced polyurethane (PU) and polystyrene (PS) membranes.[14] In our experiments we have used as-prepared (AP)-SWNTs and soluble ester-functionalized SWNTs (s-SWNT-$COO(CH_2)_{11}CH_3$, EST) in order to study the effect of the nanotube functionalization on the performance of the SWNT composites.

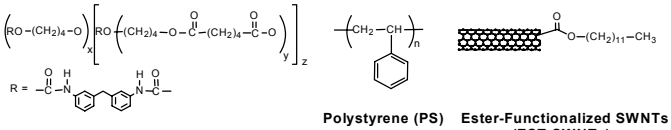

The membranes fabricated by electrospinning of the ester-functionalized SWNT-PU composite have shown enhanced mechanical properties (Table 1).[14] The increased strength exhibited by the polyurethane-SWNT-ester composites, may be due to improved dispersion of the SWNTs, but could also be a response to the polar functionalities in the SWNT-ester groups, to the opportunities offered by hydrogen bonding sites between the polymer and matrix or to amidation reactions between free amine in the polyurethane and the ester functionality in SWNTs.

Table 1. Mechanical Properties of Electrospun PU Membranes.

Electrospun membrane	Tensile strength, MPa	Tangent modulus, MPa
PU	7.02	6.96
AP-SWNT-PU*	10.26	21.86
EST-SWNT-PU*	14.36	24.32

* the SWNT:PU weight ratio is 1:100.

Functionalization of SWNTs with biomolecules

The functionalization of SWNTs with biological molecules is a relatively new direction in exploring the chemistry of SWNTs for biosensor applications. While both covalent[8,15,16] and non-covalent functionalization[17,18] with proteins, enzymes and DNA has been attempted, the covalent approach provides better stability and reproducibility of the devices fabricated from these materials.

One approach for covalent binding of proteins and enzymes utilizes the diimide-activated amidation of carboxylic acid-functionalized carbon nanotubes. We have functionalized purified SWNTs, produced by the arc-discharge method, with bovine serum albumin (BSA) as schematically illustrated in Scheme 2. The SWNT

purification process involves reflux of SWNTs in HNO_3, which terminates the open nanotube ends with carboxylic acid groups. The carboxylic groups can further undergo an amidation reaction with the amino acids of the protein.

EDC – 1-ethyl-3-(3-dimethylaminopropyl) carbodiimide hydrochloride

Scheme 2. Synthesis of BSA-functionalized SWNTs.

The BSA-functionalized SWNTs were separated from the free BSA molecules by dialysis against deionized water for 5 days. A typical AFM image of the BSA-functionalized SWNTs is given in Figure 3.

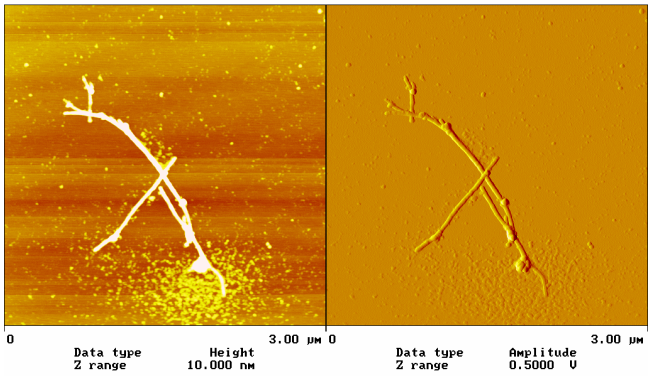

Figure 3. AFM image of BSA-functionalized SWNTs.

In order to test the biological activity of the attached the nanotubes BSA, the functionalized SWNTs were incubated in a solution of anti-BSA, developed in rabbit, for 1 hour to obtain a specific antibody-antigen interaction. The material was washed 5 times with a buffer solution (pH=7.4) and exposed to FITC-conjugated anti-rabbit IgG- for 20 min. Detection of analyte binding to the functionalized SWNTs was then performed by fluorescence and phase contrast microscopy (Figure 4).

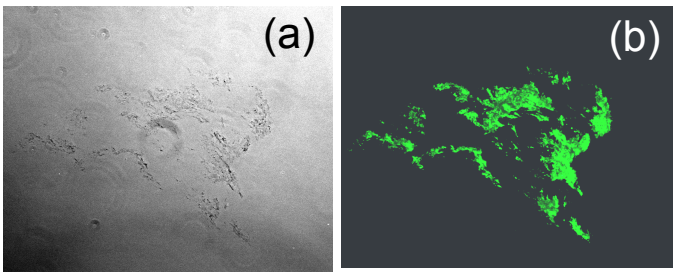

Figure 4. Phase contrast (a) and fluorescent (b) images of BSA-functionalized SWNTs.

The fluorescent image (Figure 4b) confirms the successful interaction between the BSA-functionalized SWNTs and the FITC-conjugated secondary antibody, which is an indication for the retained biological activity of the protein after the attachment to SWNTs. The fluorescent image reveals a feature similar to that observed in the phase contrast image (Figure 4a). A control test with non-functionalized SWNTs incubated in FITC-conjugated anti-rabbit IgG resulted in a dark image, which confirming the specific interaction between the BSA-functionalized SWNTs and anti-BSA. These specific interactions may be used for development of biosensors and controlled assembly of ordered nanostructures.

Conclusions.

The chemistry of SWNTs offers considerable scope for development of functional materials, structures and devices based on SWNTs. Further advance in our understanding the chemistry of SWNTs will make it possible to take full advantage of the remarkable properties of these materials and will help to tailor the properties of SWNTs for particular applications.

Acknowledgement. This work was supported by DOD/DARPA/DMEA under Award No. DMEA90-02-2-0216.

References

(1) Chen, J.; Hamon, M. A.; Hu, H.; Chen, Y.; Rao, A. M.; Eklund, P. C.; Haddon, R. C. *Science* **1998**, *282*, 95-98.
(2) Chen, Y.; Haddon, R. C.; Fang, S.; Rao, A. M.; Eklund, P. C.; Lee, W. H.; Dickey, E. C.; Grulke, E. A.; Pendergrass, J. C.; Chavan, A.; Haley, B. E.; Smalley, R. E. *J. Mater. Res.* **1998**, *13*, 2423-2431.
(3) Holzinger, M.; Vostrowsky, O.; Hirsch, A.; Hennrich, F.; Kappes, M.; Weiss, R.; Jellen, F. *Angew. Chem., Int. Ed.* **2001**, *40*, 4002-4005.
(4) Dyke, C. A.; Tour, J. M. *Nano Lett* **2003**, *3*, 1215-1218.
(5) Saini, R. K.; Chiang, I. W.; Peng, H.; Smalley, R. E.; Billups, W. E.; Hauge, R. H.; Margrave, J. L. *J. Am. Chem. Soc.* **2003**, *125*, 3617-3621.
(6) Dyke, C. A.; Tour, J. M. *J. Am. Chem. Soc.* **2003**, *125*, 1156-1157.
(7) Haremza, J. M.; Hahn, M. A.; Krauss, T. D.; Chen, S.; Calcines, J. *Nano Lett* **2002**, *2*, 1253-1258.
(8) Williams, K. A.; Veenhuizen, P. T. M.; de la Torre, B. G.; Eritja, R.; Dekker, C. *Nature* **2002**, *420*, 761.
(9) Niyogi, S.; Hamon, M. A.; Hu, H.; Zhao, B.; Bhowmik, P.; Sen, R.; Itkis, M. E.; Haddon, R. C. *Acc. Chem. Res.* **2002**, *35*, 1105-1113.
(10) Kamaras, K.; Itkis, M. E.; Hu, H.; Zhao, B.; Haddon, R. C. *Science* **2003**, *301*, 1501.
(11) Chen, J.; Rao, A. M.; Lyuksyutov, S.; Itkis, M. E.; Hamon, M. A.; Hu, H.; Cohn, R. W.; Eklund, P. W.; Colbert, D. T.; Smalley, R. E.; Haddon, R. C. *J. Phys. Chem. B* **2001**, *105*, 2525-2528.
(12) Zhao, B.; Hu, H.; Haddon, R. C. *Adv. Func. Mater.* **2004**, *14*, 71-76.
(13) Hu, H.; Ni, Y.; Montana, V.; Haddon, R. C.; Parpura, V. *Nano Letters* **2004**, *4*, 507-511.
(14) Sen, R.; Zhao, B.; Perea, D. E.; Itkis, M. E.; Hu, H.; Love, J.; Bekyarova, E.; Haddon, R. C. *Nano Lett.* **2004**, *4*, 459-464.
(15) Dwyer, C.; Guthold, M.; Falvo, M.; Washburn, S.; Superfine, R.; Erie, D. *Nanotechnology* **2002**, *13*, 601-604.
(16) Huang, W.; Taylor, S.; Fu, K.; Lin, Y.; Zhang, D.; Hanks, T. W.; Rao, A. M.; Sun, Y.-P. *Nano Lett.* **2002**, *2*, 311-314.
(17) Chen, R. J.; Zhang, Y.; Wang, D.; Dai, H. *J. Am. Chem. Soc.* **2001**, *123*, 3838-3839.
(18) Dieckmann, G. R.; Dalton, A. B.; Johnson, P. A.; Razal, J.; Chen, J.; Giordano, G. M.; Munoz, E.; Musselman, I. H.; Baughman, R. H.; Draper, R. K. *J. Am. Chem. Soc.* **2003**, *125*, 1770-1777.

GOLD AND ALLOY NANOPARTICLE CATALYSTS IN FUEL CELL REACTIONS

*Mathew M. Maye, Jin Luo, Li Han, Nancy Kariuki, Zia Rab, Navaid Khan, H. Richard Naslund and Chuan-Jian Zhong **

Department of Chemistry
State University of New York at Binghamton
Binghamton, NY 13902 (*cjzhong@binghamton.edu)

Introduction

Gold-based nanoparticles (1-5 nm) have recently emerged as highly active catalysts for many important catalytic reactions [1]. A major factor for their catalytic activity is related to the size- and composition-dependent properties of nanoparticles. We have investigated the preparation and catalytic properties of gold-based alloy nanoparticles supported on carbon materials [2,3]. One example involves the preparation of monolayer-capped AuPt nanoparticles for electrocatalytic oxidation of methanol and reduction of oxygen. To delineate the size and composition correlation of the catalytic properties, we employed an array of surface analytical techniques to probe the structural and morphological evolution and reconstitution of the nanoparticles upon catalytic activation. These techniques include; atomic force microscopy (AFM), transmission electron microscopy (TEM), surface infrared reflection spectroscopy (IRS), X-ray photoelectron spectroscopy (XPS), and thermogravimetic analysis (TGA) [3-5]. The combined results of these characterizations have provided insights into the viability of tailoring the nanostructured catalysts in terms of size and composition.

Experimental

Gold nanoparticles (Au) of 2-nm core size encapsulated with alkanethiolate monolayer shells (e.g. decanthiol, DT) were synthesized by the standard two-phase method [6]. Gold-platinum (AuPt) nanoparticles of 2-nm core size encapsulated with an alkanethiolate monolayer shell (AuPt) were synthesized by a modified two-phase method. The Au:Pt ratio in the nanoparticles controlled in synthesis and analyzed using the direct current plasma – atomic emission spectroscopy method.

Au and AuPt nanoparticles were loaded on XC-72 carbon black, and were treated in a tube-furnace under controlled temperatures and atmospheres. For catalytic activity measurements, suspensions of the catalysts (AuPt/C) with Nafion were quantitatively cast to the surface of the polished GC disk.

The cyclic voltammetry (CV) experiments were performed at room temperature. All experiments were performed in three-electrode electrochemical cells, and electrolytic solutions were deaerated with high purity argon or nitrogen before the measurement. All potentials are given with respect to the reference electrode of Ag/AgCl saturated KCl. The measurements were performed using a microcomputer-controlled potentiostat (M273, PARC).

Results and Discussion:

Figure 1 showed a set of IRS for DT capped Au. Before thermal activation at 250 ^{o}C (30 min, O_2) the C-H stretching bands from the encapsulating DT are detected. Upon thermal treatment, these bands disappeared to a level below the detection limit, demonstrating the removal of the organic shell. The shell removal can also be correlated with recent TGA and in-situ heating AFM characterization. The shell removal was also confirmed by XPS, which showed the removal of S species.

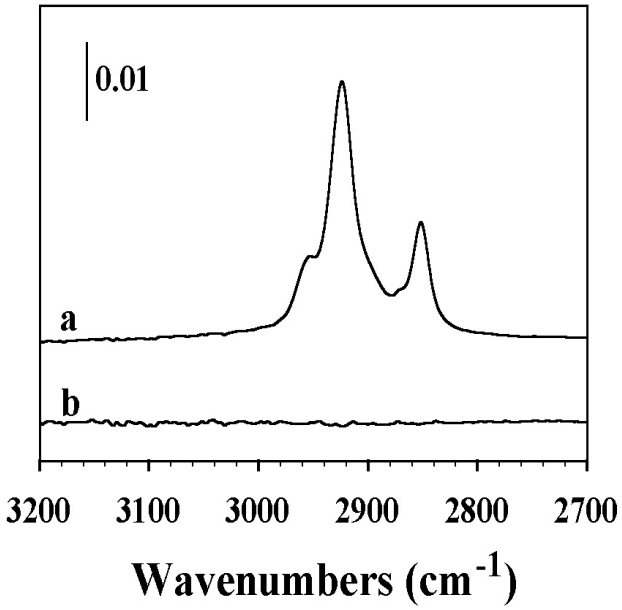

Figure 1. IRS spectra for DT-capped Au nanoparticles in the C-H stretching region before (a) and after (b) thermal treatment at 250 ^{o}C for 30 min.

By AFM characterization, we recently showed that at low surface coverages there were some degree of local aggregation of the Au nanoparticles depending on the nature of the substrate (from ~2 nm to 5~6 nm), but the resulting particle sizes are controllable. Similar results have also been observed with Au-containing bimetallic nanoparticles.

Figure 2 shows a set of CV data for the electrocatalytic reduction of oxygen at $Au_{81}Pt_{19}$/C catalyst in alkaline solutions. The catalyst were thermally treated, and the total metal loading was ~20% wt. The data were also compared with data for Pt/C catalyst (20%wt, E-tek) (not shown). Similar to the CV curve for the Au/C catalyst in the absence of oxygen (not shown), the observation of the oxidation-reduction wave of gold oxide at ~200 mV at the $Au_{81}Pt_{19}$/C catalyst in the O_2-free alkaline electrolyte is a clear indication of the presence of Au on the catalyst. The observation of the hydrogen reduction-oxidation currents at –200 mV in the O_2-free acidic electrolyte is strong evidence for the presence of Pt on the catalyst surface. In comparison with the data for Au/C catalysts, there are two important observations for the electrocatalytic activity of the AuPt nanoparticle catalysts. First, the ORR wave at the $Au_{81}Pt_{19}$/C catalyst is observed at about the same potential (+190 mV) as that for the Au/C in the alkaline electrolyte. We also note that a very small wave is detectable at –450 mV for the AuPt/C catalyst. Second, the ORR wave is highly dependent on the nature of the electrolyte. This

wave for $Au_{81}Pt_{19}$/C is observed at +350 mV in the acidic electrolyte, which is much more positive than that for the Au/C (+50 mV) in the same electrolyte. The result thus suggests that there is a significant fraction of Au on the bimetallic catalyst which keeps the nanoscale gold property unchanged in basic condition, but modifies the catalytic property of Pt in the acidic electrolyte.

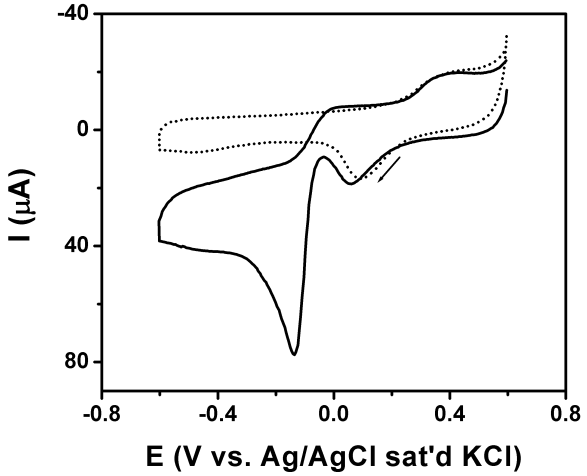

Figure 2. CV curves for a $Au_{81}Pt_{19}$/C catalyst (20%wt) on GC electrode (0.07 cm^2) in 0.5M KOH. The electrolytes were saturated with O_2 (solid curve) and Ar (dash curve). Scan rate: 50 mV/s.

The dependence of the electrocatalytic activity on the relative bimetallic composition of the catalyst is currently under investigation. We have shown that Au and AuPt nanoparticles that are highly active catalysts for fuel cell reactions can be prepared a combination of synthesis and processing strategies. The study of the tunability of the catalytic activities in terms of size and composition is part of our on-going investigation.

Acknowledgement

This work was supported in part by the National Science foundation, the Petroleum Research Fund administered by the American Chemical Society, and the GROW fund of the World Gold Council. M.M.M. thanks the Department of Defense for the National Defense Science & Engineering Graduate Fellowship support sponsored by ARO.

References

(1) Zhong, C.J.; Maye, M. M.; Luo, J.; Han, L.; Kariuki, N. N.; in "Nanoparticles: Building Blocks for Nanotechnology," Ed. By Rotello, V.M.; Kluwer. 2004. pp.113-144
(2) Zhong, C. J.; Luo, J.; Maye, M. M.; Han, L.; Kariuki, N. N.; in "Nanotechnology in Catalysis," Ed. Zhou, B.; Hermans, S.; Somorjai, G. A.; Kluwer, 2004; Vol 1., pp. 222-248.
(3) Luo, J.; Maye, M. M.; Lou, Y.; Han, L.; Hepel, M.; Zhong, C. J.; *Catal. Today*, **2002**, *77*, 127
(4) Maye, M.M.; Luo, J.; Lin, Y.; Engelhard, M.H.; Hepel, M.; Zhong, C.J.; *Langmuir*, **2003**, *19,* 125
(5) Maye, M.M.; Luo, J.; Han, L.; Kariuki, N. N.; Zhong, C.J.; *Gold Bull*., **2003**, *36*, 75
(6) Brust, M.; Walker, M.; Bethell, D.; Schiffrin, D. J.; Whyman, R. *J. Chem. Soc., Chem. Comm*. **1994**, 801.

HYDROFORMYLATION OF 1-OCTENE OVER CARBON NANOTUBE SUPPORTED COBALT CATALYST

Jieshan Qiu, Hongzhe Zhang, Xiuna Wang, Bing Yin

Carbon Research Laboratory, School of Chemical Engineering, Center for Nano Materials and Science, State Key Laboratory of Fine Chemicals, Dalian University of Technology, 158 Zhongshan Road, P.O .Box 49, Dalian 116012, China. E-mail: jqiu@dlut.edu.cn; Fax: +86-411-3633080

Introduction

The hydroformylation of higher olefins (also known as oxo process or carboxylation) is one important process for making value-added precursors or intermediates of chemicals and medicines, in which both homogeneous and heterogeneous catalysts have been extensively studied [1-4]. Recently, hydroformylation over carbon materials supported catalysts has drawn much attention [3-7], showing that carbon-supported catalysts are more active than the oxide-supported catalysts. Apart from the common knowledgement that carbon materials are a good electron-transfer agent, it is also found that carbon materials favor the carbonylation reactions because of their unique roles in the reactions, including to suppress dissociative hydrogen adsorption, to promote strong or multiple adsorption of CO and to inhibit dissociative CO adsorption [4]. These special characteristics of carbon materials are also important for hydroformylation reactions, which are governed by the molecular reaction of CO. Carbon nanotubes (CNTs) is a novel nano-sized carbon and is believed to be of potential as catalyst support for heterogeneous catalysis. Some studies about the hydroformylation of olefins over the CNTs-supported catalysts [5-7] have proved that the CNTs-supported catalysts are indeed quite active for the hydroformylation of olefins that involves a sequence of several competitive parallel and consecutive reactions. In the present work, the hydroformylation of 1-octene over CNT-supported cobalt catalysts were studied, and the variation of the activity and selectivity of the catalysts in different solvents and with the reaction time were analyzed. The reaction conditions were optimized with an aim of producing C_9-aldehyde selectively.

Experimental

The raw CNTs (RCNTs) was prepared by arc-discharge of high purity graphite electrodes, and was further treated by refluxing 65% HNO_3 at 120 ^oC for 8 h to obtain purified CNTs (PCNTs). Co/CNTs was prepared by incipient wetness impregnation technique with an aqueous solution of cobalt nitrate. After impregnation, the samples were dried overnight at 110 ^oC and calcined in air at 400 ^oC for 3 h, then, were reduced in flowing hydrogen at 400 ^oC for 6 h. Finally, the catalysts were passivated by 1% O_2 in N_2 at room temperature for 3 h. The reaction of 1-octene hydroformylation was conducted in a magnetically stirred autoclave with an inner volume of 100 ml and at 130 ^oC in high purity syngas (H_2/CO=1:1) with initial pressure being 5.0MPa. For each run, the reactor was loaded with 40 ml of solvent containing 13.4 mmol (15 g) of 1-octene and 100 mg of catalysts. After the reaction was finished, the products were analyzed using GC-MS (HP6890GC/5973MSD). Both the raw CNTs samples and the CNTs-supported catalysts were examined by transmission electron microscopy (TEM, JEOL JEM-2000EX, operated at 100 kV).

Results and Discussion

The solvent is an essential parameter that needs to be considered for liquid phase hydroformylation. The hydroformylation of 1-octene over 5.0 wt% Co/PCNTs were conducted in three different solvents, i.e. cyclohexane, acetone and ethanol, of which the data are presented in **Table 1.** It can be seen from Table 1 that in the case of cyclohexane, aldehydes are the only products, i.e. the selectivity of C_9-aldehyde is 100%, but the conversion of 1-octene is very low, only 9.37%. While in the case of acetone and ethanol solvent, the catalyst performance is improved significantly. For the acetone solvent, 52.3% 1-octene is converted with the selectivity of C_9-aldehyde being 95.30%. For the ethanol solvent, the conversion of 1-octene is 57.35% with the selectivity of C_9-aldehyde being only 9.21%, in this case condensation reactions take place that results in acetal products (C_{19}/C_{20}). Obviously, the acetone and ethanol solvents favor the reaction of 1-octene hydroformylation. This is in agreement with previously reported result [3]. This phenomenon may be attributed to the following factors: the reduction of cobalt catalyst is easier in ethanol than in cyclohexane; the formation of acetal and hemiacetals favors chem-equilibrium reaction that leads to aldehyde products, which help to speed up the reaction of hydroformylation; some solvent molecules may be adsorbed on the catalyst, which modifies the catalyst's surface.

Table 1. Effect of Solvents on Hydroformylation of 1-Octene[a]

Solvents	Conversion of 1-octene (%)	Selectivity (%)		
		C_9-aldehyde	C_9-alcohols	C_{19}/C_{20} acetal
Cyclohexane	9.67	100	0	0
Acetone	52.3	95.30	0	4.70
Ethanol	57.35	9.21	31.42	58.37

[a] reaction conditions: 130 ^oC, 5.0 MPa, 6 h.

Table 2. Effect of Reaction Time on 1-Octene Hydroformylation[a]

Time (h)	1-octene conversion (%)	C9-aldehyde Selectivity(%)	n/i
4	0	0	0
5	9.95	91.36	5
6	52.3	74.3	0.94
7	53.4	56.9	0.53
8	52.6	54.2	0.29

[a] reaction conditions: 130 ^oC, 5.0 MPa, 40 ml acetone

The variation of the 1-octene hydroformylation with the reaction time is shown in **Table 2.** It can be seen from Table 2 that the conversion of 1-octene increases as time increases, then levels off after 6 h, at the same time, the selectivity of C_9-aldehyde drops and the ratio of n/i becomes smaller as the reaction time increases. The detailed reason for this phenomenon is not clear at the moment. It is very likely due to the complex reaction scheme involved in the reaction system, in which some competitive and consecutive reactions take place. The decrease in the n/i ratio can be attributed to the steric effect for the insertion of CO in the second C atom of the 1-octene that is relatively difficult in comparison to the insertion of CO in the first C atom, which makes the formation of linear products go faster than the branched ones. However, the decrease of n/i ratio might also be due to the decrease of CO partial pressure as the reaction proceeds. More CO species on the metal catalysts at high pressures is favorable for the formation of linear products rather than branched ones.

In addition, a peculiar metal/support interaction between the cobalt crystallites and the CNT support could have a significant influence on the conversion of 1-octene and product selectivity in comparison to active carbon-supported catalyst. Such a hypothesis has been evidenced by the specific selectivity observed over graphite nanofiber-supported catalyst: a significant improvement in the selectivity has been reported by Baker and his colleagues [6] with the use of graphite nanofiber as support during the liquid phase hydrogenation of cinnamaldehyde.

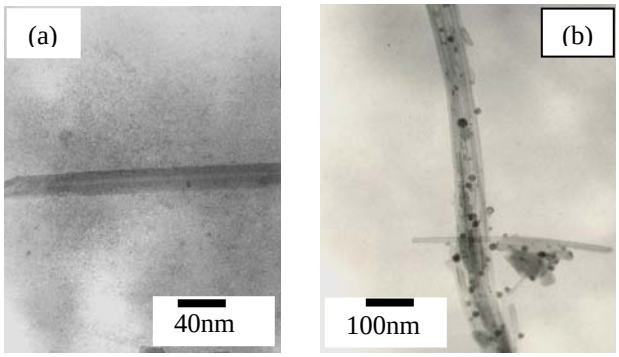

Figure 1. TEM images of CNTs samples; (a) the PCNTs, (b) the Co/PCNTs catalyst.

The CNTs materials before and after acid treatment were examined using TEM, and fairly clean CNTs and the agglomeration of few carbonaceous impurities in the bulk can be observed after purification treatment. It has been found that the outer diameters of PCNTs are in a range of 6-50 nm, and the inner diameters are in a range of 3-5 nm. The typical TEM image of the PCNTs sample is shown in **Fig. 1a**. The BET surface area of the CNTs, determined by nitrogen adsorption at 77 K, is about 22.5m^2/g.

Fig. 1b shows a typical TEM image of Co/PCNTs catalyst. From the TEM images, the size of metal catalysts and the size distribution can be measured and calculated. It can be seen clearly that the metal catalysts, the dark spots on the external surface of the tubes, are uniformly deposited on the surface of CNTs, though occasionally some large aggregates can also be seen. For Co/PCNTs catalysts, the size of metal Co particles are in a range of 10-15nm. The relatively homogeneous dispersion could be attributed to the relatively strong metal/support interaction between the metal salt precursor and the carbon nanotubes [6]. Baker et al reported that the distribution of metallic particles size on the graphite nanofibers was relatively wide, ranging from 1.5 nm to 43.5 nm, with an average size of *ca.* 7-10 nm; nickel particles were deposited on the external surface of the nanotubes; and the nickel supported on the nanofiber surface adopted a peculiar thin hexagonal morphology and almost no spheroidal particles were observed. This means that depending on the nature of the support, the morphology of the metal particles can be modified during the preparation step. The difference between the present work and Baker's work could be attributed to the different crystallinity of the two carbon supports, which could influence the formation of the final metal morphology.

Under the identical experiemtnal conditions, the performance of Co catalysts supported on CNTs and a kind of active carbon was also compared, of which the results are shown in Table 3. It can be seen from Table 3 that the CNTs-supported Co catalyst is more active than the AC supported Co catalyst. This might be due to the good crystallinity of the CNTs support, and it needs to be clarified in detail.

Table 3. Comparison of the Catalytic activity of PCNTs and Active carbon supported Co catalysts [a]

Catalyst	1-octene conversion (%)	C_9-aldehyde Selectivity(%)	n/i
Co/PCNTs	41.54	71.56	0.96
Co/AC	24.26	33.38	0.68

[a] reaction conditions: 130 ^oC, 5.0 MPa, 40 ml acetone

In summary, the performance of Co/CNTs for the 1-octene hydroformylation varies greatly in different solvents. Under the reaction conditions mentioned above, 6 h is suitable for the hydroformylation of 1-octene. Thus, for the liquid phase hydroformylation of 1-octene, rational design of catalysts and optimized reaction conditions are essential to the CNTs-supported catalysts. In this regard, more detailed work is needed.

Acknowledgment. This work was partly supported by the National Science Foundation of China (No. 29976006, 20376011), the Natural Science Foundation of Liaoning Province (No. 9810300701, 2001101003), the National Basic Research Program of China (Grant No. G2003CB615806) and the Ministry of Education of China.

References

(1) McDougall, J.K.; Simpson, M.C.; Green, M.J.; *J. Chem. Soc., Dalton Trans.* 1996, 1161.
(2) Qiu, X.; Tsubaki, N.; Sun, Shouli; Fujimoto, K.; *Catalysis Communications*. 2001, (2) 75.
(3) Li, B.T.; Li, X.H.; Asami, K.; Fujimoto, K.; *Chemistry Letters.* 2003, 32, 378.
(4) Kainulainen, T.A.; Niemelä, M.K.; Krause, A.O.I.; *Journal of Molecular Catalysis A: Chemical.* 1997, 122, 39.
(5) Planeix, J.M.; Coustel, N.; Coq, B.; Brotons, V.; Ajayan, P.M.; *J. Am. Chem. Soc.* 1994,116, 7935.
(6) Zhang, Y.; Zhang, H.-B.; Lin, G.-D.; Chen, P.; Yuan, Y.-Z.; Tsai, K. R.; *Appl. Catal. A.* 1999, 187, 213.
(7) Baker, R.T.K.; Laubernds, K.; Wootsch, A.; Paal, Z.; *J. Catal.* 2000, 193, 165.

ON THE HYDROGEN ON-BOARD STORAGE IN GRAPHITE NANOMATERIALS

Yury S. Nechaev[1] and T. Nejat Veziroglu

Clean Energy Research Institute, College of Engineering, University of Miami, Coral Gables, FL 33124; [1)] Fulbright grantee (Moscow)

Introduction

As is noted in study[1], there is the anomalous scattering and non-reproducibility of the known experimental data on the hydrogen gravimetric capability in carbon nanofibers and nanotubes (3 orders of magnitude, if the unique Rodriguez-Baker data[2] are included, and 2 orders, if without them), while there is a 'normal' scattering (within one order of magnitude) – for metallic hydrides (practically, in studies of the same researches).

According to our feeling, the main reasons of such a large difference in the results are related with a larger spectrum of the structure and sorption process peculiarities for the carbon nanomaterials (in comparison with metallic hydrides), depending on regimes of their synthesis, pre-treatment and hydrogenation, and also on their composition (particularly, with respect to metallic catalysts).

In this connection, some new significant results on diffusion, sorption and storage of hydrogen in graphites and novel carbon nanomaterials are discussed, which have been obtained on the basis of thermodynamic analysis[3-7] of the known experimental data, and their comparison with theoretical data[8] (*'ab initio'* molecular orbital (MO) studies of chemisorption of hydrogen atoms on graphite).

Results and Discussion

According to analysis[4-7], in many cases the main processes of hydrogen desorption both in an isotropic graphite[9] (TPD peaks I, II, III, IV) and in novel carbon nanomaterials with sp^2 hybridization can be characterized as trapping-with-diffusion rate-controlled processes with the diffusion activation enthalpies of $Q_I \approx 20$ kJ/mol ($H_{2(ads)}$), $Q_{II} = 120$ kJ/mol ($H_{2(ads)}$), $Q_{III} = 250$ kJ/mol ($H_{(abs)}$), $Q_{IV} \approx 365$ kJ/mol ($H_{(abs)}$), corresponding to the related desorption enthalpies (due to the reversible diffusant trapping by carbon chemisorption "sites"). The entropy (frequency) factors of the hydrogen diffusion coefficients in these materials have also been determined[4-7]: $D_{0I} \approx 0{,}003$ cm^2/s, $D_{0II} = 1800$ cm^2/s, $D_{0III} \approx 0{,}007$ cm^2/s, $D_{0IV} \approx 600$ cm^2/s.

TPD peak III in the isotropic graphite[9] is related with a dissociative chemisorption of H_2 gas molecules on carbon chemisorption sites localized in graphene layers in grains-crystallites, and corresponding to potential "HC- molecules" (within model[8] 'F', sp^3 rehybridization). The total process III is described by an absorption isotherm of the Sieverts-Langmuir type: $((X_{III}/X_{IIIm}) = K_{III}(P_{H2}/P^0_{H2})^{1/2} / [1+K_{III}(P_{H2}/P^0_{H2})^{1/2}]$, $K_{III} = \exp(\Delta S_{III}/R)\exp(-\Delta H_{III}/RT)$, where $P^0_{H2} = 1$ Pa, the absorption enthalpy of $\Delta H_{III} = -19$ kJ/mol ($H_{(abs..)}$); the absorption entropy of $\Delta S_{III} \approx -(14{,}7\text{-}15{,}4)R$; the largest potentially possible concentration of hydrogen atoms (H/C) in graphene layers of $X_{IIIm} = 0{,}5\text{-}1{,}0$, that is close to the hydrogen content in "a carbohydride-like bulk phase".

The process (III) includes the first stage (1) of hydrogen molecules dissociation to atoms with enthalpy of $\Delta H_{(1)} = 228$ kJ/mol ($H_{(gas)}$), the second stage (2) of hydrogen atoms dissolution between graphene layers with $\Delta H_{(III2)} \approx 0$, and the third stage (3) of hydrogen atoms chemisorption on "HC-sites" with $\Delta H_{(III3)} = -247$ kJ/mol($H_{(abs.)}$); $\Delta H_{III} \approx (\Delta H_{(1)}+\Delta H_{(III3)})$. Thus, TPD peak III in graphite[9] is related with the trapping-with-diffusion of hydrogen atoms in grains-crystallites, with the reversible diffusant trapping (chemisorption) by "HC-sites" in graphene layers; $Q_{III} \approx -\Delta H_{(III3)}$.

According to analysis[4-7], the concentration of hydrogen absorbed in graphene layers (TPD peak of III type) in nanostructured graphite[10] and in graphite nanofibers[2] can be close to the largest possible ("carbohydride-like") values (X_{IIIm}).

The sorption capability of TPD peak of III type in carbon nanofibers and mechanically prepared nanostructured graphite charged under P_{H2} = 1-10 MPa and room temperatures can be close to the values ($X_{III} \approx 0.5\text{-}0.8$), corresponding to the technical targets for hydrogen storage on-board fuel cell-powered vehicles; however, the near-zero "reversibility" (i.e., a very sluggish diffusion kinetics) of the process is not acceptable.

Ab initio MO calculations[8] (model 'F') give the chemisorption energy of hydrogen atoms in the graphene layers of about -195 kJ/mol (H_{abs}), i.e., the absolute value is considerably less than for $\Delta H_{(III3)}$. It points to the necessity of the further theoretical[11,12] and experimental studies (in the light of results[4-7]) of this contradiction, that has a significant importance in the connection with the graphene structure of carbon nanotubes and nanofibers.

TPD peak IV in isotropic graphite[9] is related with a dissociative chemisorption of H_2 gas molecules on 'armchair' and/or 'zigzag' edge carbon sites localized mainly near the grain boundary regions and corresponding to potential "HC-like molecules" (within model[8] 'C' and/or 'D' sp^2 hybridization). Total process (IV) is described [4-7] by a sorption isotherm of the Sieverts-Langmuir type , with $\Delta H_{IV} \approx -140$ kJ/mol ($H_{(abs..)}$); $\Delta H_{(IV3)} \approx (\Delta H_{IV} - \Delta H_{(1)}) \approx -Q_{IV}$. The sorption capacity and the diffusion kinetics ("reversibility") of this peak at room temperatures and technological pressures do not satisfy to the hydrogen vehicles target values.

TPD peaks II and I in isotropic graphite[9] are related with a dissociative-associative chemisorption of H_2 gas molecules on carbon sorption sites localized in the regions of grain-crystallites boundaries and boundaries (interfaces) of graphite filler grains, and corresponding to potential "H_2C-molecules" (within model[8] 'H' of 'zigzag' edge sp^3 rehybridization sites (for TPD peak II) and model[8] 'G' of 'armchair' edge sp^3 rehybridization sites (for TPD peak I), and also (another variant for peak I) - to potential "H_2C_2-molecules" (within model[8] 'F' of sp^3 rehybridization in graphene sites). Total process is described[4-7] by a sorption isotherm of the Henry-Langmuir type: $((X/X_m) = K(P_{H2}/P^0_{H2}) /[1+K(P_{H2}/P^0_{H2})]$, $K = \exp(\Delta S/R)\exp(-\Delta H/RT)$, with adsorption enthalpies and entropies values of $\Delta H_{II} \approx -Q_{II}$, $\Delta H_I \approx -Q_I$, $\Delta S_{II} \approx -31R$, $\Delta S_I \approx -23R$, and the largest potentially possible concentrations (H_2/C_{loc}) close to the hydrogen content in "a carbohydride-like adsorbed phase". TPD peaks II and I are related with the trapping-with-grain boundary diffusion of hydrogen molecules, with reversible trapping (chemisorption) of the diffusant by "$H_2C(H_2C_2)$ sites"; the apparent activation enthalpies of the hydrogen diffusion can be close to the desorption enthalpies.

The sorption capabilities (H/C_{tot}) of TPD peaks of II and I types in carbon nanostructures ($2\gamma_{II}X_{II}$ and $2\gamma_I X_I$, where γ_{II} and γ_I are the volume fractions of the sorption regions) can be close to the values (~0.8), corresponding to the technical targets for hydrogen storage on-board fuel cell vehicles; however, the near-zero "reversibility" (the diffusion kinetics) of the II type peak is not acceptable, and moreover, the nature, characteristics and conditions of the manifestation of the I type peak in carbon nanotubes and nanofibers have been insufficiently studied.

A specific physical (or physicochemical) multilayer hydrogen adsorption, with an anomalous high sorption capacity and adsorbate packing density ("peak V"), seems to be possible in graphite nanofibers[2], which (according to analysis[4-7]) could be "decorated" with "the carbohydride-like phases" (TPD peaks of the II and III types). There are serious reasons[4-7] to suppose that the sorption capacity and "reversibility" (kinetics) of this nearly unstudied

process ("peak V") can satisfy to the technique requirements for the hydrogen on-board storage in fuel cell-powered vehicles.

On chemiadsorption and chemiabsorption of hydrogen by isotropic graphite, mechanically nanostructured graphite and graphite nanofibers. As is noted in study[13], one of the main reasons for the negative discussion of the anomalous scattering and non-reproducibility of some known experimental data on the hydrogen gravimetric capability in carbon nanofibers and nanotubes is confusion in the gas storage concepts: physical adsorption, chemisorption, absorption and occlusion. As is also noted[13], physical adsorption and chemisorption are surface phenomena, and in absorption and occlusion, the material taken up is distributed through the body (bulk) of the absorbent.

According to our feeling, some additional aspects (concepts) must be taken into account on evaluating the storage capacity, as follows[4-7,11].

1. Absorption (in the sense of a true bulk solubility) can be attributed with the thermodynamic characteristics of the gas (adsorbat) interaction with the normal lattice of the absorbent, and it can be of a chemical nature; a situation of a dissociative chemiabsorption has obviously place for hydrogen sorption processes, corresponding to TPD peak of # III type in isotropic graphite, mechanically nanostructured graphite and graphite nanofibers. 2. Adsorption (especially, of a chemical nature) can be attributed with the thermodynamic characteristics of the gas interaction with the free surface regions (nanolayrs), both external and internal ones (as pore and cavity surfaces), grain boundary regions (nanolayers) or near dislocation nanoregions in the adsorbent bulk; a situation of a dissociative-associative chemiadsorption has obviously place for processes, corresponding to TPD peaks of # II type in the three materials mentioned above. 3. The sorption process, corresponding to the extremely anomalous 'peak' # V in the Rodriguez-Baker graphite nanofibers[2], might be related with a specific physico-chemical hydrogen adsorption[4-7], that is a subject of further studies.

On the nature of the catalyst activity of nanostructured graphite, under ball milling in hydrogen molecular gas atmosphere. As has been mentioned above, thermodynamic and diffusion characteristics of two hydrogen desorption processes (similar to the processes of TPD peaks # II and # III) are obtained from data[10] on mechanically prepared nanocrystalline graphite charged at P_{H2} = 1 MPa and about 300 K (under the ball milling). It's necessary to emphasize result[4-7], that the concentrations of both the chimiabsorbed and the chemiadsorbed hydrogen in the mechanically nanostructured graphite are of the same order as the largest possible (carbohydride-like) values and correspond to the extrapolated (equilibrium) values, those are obtained by the use of the isotherms noted above (for TPD peaks # II and # III).

Hence, it follows that the catalyst activity of the ball milling graphite results in the sufficiently fast kinetics of the intermediate step of H_2 dissociation, which occurs over the carbon catalyst. Such a high catalyst activity of the milling graphite is obviously caused by a high stationary concentration of the lattice defects in the material[14]; some of them are attributed with the formation of the dangling C-C sp^2 edge bonds of the zigzag-like or armchair-like types. The nature of the catalyst activity of the ball milling graphite is revealing by the comparison of the absolute values of the H_2 dissociation energy and the adsorption (absorption) energies of atomic hydrogen on the different carbon sites (C-H, C-2H bonds energies), and especially on the sites related with the deformation lattice defects (in the deforming graphite).

Conclusions

Thermodynamic analysis[4-7] of some known data on hydrogen sorption in by novel carbon nanomaterials allows us to suppose that the anomalous large scattering (up to three orders of the magnitude) in the experimental values of the hydrogen capacity at room temperatures and the technological pressures in the studies of different authors is mostly related with faintly studied physicochemical aspects (processes).

The presented results[4-7] are mainly of the conceptual and methodological significance, and they can serve as an effective basis both for the further fundamental and technological developments on using novel carbon nanomaterials in the field of hydrogen energy for vehicles. Such new results are important for optimizing and understanding the interaction between hydrogen and carbon materials[15].

There is a real possibility of revealing the true Rodriguez-Baker regimes of hydrogenation and/or synthesis of graphite nanofibers, providing the manifestation of the anomalous 'peak V', and their use for a radical solution of the urgent problem of the hydrogen on-board storage – a bottle neck in constructing fuel cell-powered non-pollution vehicles.

References

1. Hirscher M, Becher M, Haluska M, Chen X, Dettlaff-Weglikowska U, Roth S. *Abstracts of MH2002*, France; **2002**, 29.
2. Park C, Anderson PE, Chambers A, Tan CD, Hidalgo R, Rodriguez NM. *J. Phys. Chem. B*, **1999**,103, 10572-10581.
3. Nechaev YuS. *Physics Uspekhi*, **2001**, 171, 1251-1261.
4. Nechaev YuS, Alexeeva OK. *IJHE*, **2003**, 28, 1433-1443.
5. Nechaev YuS, Alexeeva OK. *Transactions of EHEC-2003*, Grenoble, France; **2003**, (CO2-43).
6. Nechaev YuS, Alexeeva OK, Hirschberg JG, Veziroglu TN.. *Transactions of the HYPOTHESIS V*, Porto Conte, Italy; **2003**.
7. Nechaev YuS, Alexeeva OK. *Chemistry Uspekhi*, **2004**.
8. Yang FH, Yang RT. *Carbon*, **2002;**, 40, 437-444.
9. Atsumi H, Tokura S, Miyake M. *J. Nucl. Mater*. **1988,** 155-157, 241-245.
10. Orimo S, Matsushima T, Fujii H, Fukunaga T, Maier G. *J. Appl. Phys.*, **2001**, 90, 1545-1549.
11. Stojkovic D, Zhang P, Lammert PE, Crespi VH. *Physical Review B*, **2003,** 68, 195406-1-195406-5.
12. Volpe M, Cleri F. *Surface Science*, **2003,** 544, 24-34.
13. Murata K, Kaneko K, Kanoh H, Kasuya D, Takahashi K, Kokai F, Yudasaka M, Iijima S. *J. Phys. Chem. B*, **2002,** 106, 11132-38.
14. Nechaev YuS. *Transactions (Izvestija) of the Russian Academy of Sciences, Physical Series*, **2001**, 65, 1399-1406.
15. Dillon AC, Heben MJ. *Appl. Phys. A*, **2001**, 72, 133-142.

ELECTRICAL CHARGE DISTRIBUTION STUDIES IN SWNT, C_{60}@SWNT, AND DWNT STRUCTURES

Jose Rivera[1], *G. U. Sumanasekera[1], S. Bandow[2], S. Iijima[2], P. C. Eklund[3].*

[1]Department of Physics, University of Louisville, KY 40292, U.S.A
[2]Department of Physics, Meijo University, Nagoya, Japan
[3]Department of Physics, Penn State University, University Park, PA 16802, U.S.A.

Introduction

Single walled Carbon nanotubes (SWNTs) have extremely interesting and unique chemical and physical properties. The interior space of SWNTs can be utilized for interesting applications such as one-dimensional array elements, drug delivery, and fluidics. C_{60} molecules have been inserted with high efficiency in the interior of SWNTs by vapor phase reaction of C_{60} with SWNTs to form peapods (C_{60}@SWNT). It has been found that high temperature annealing of peapods at 1200 ^{0}C result in coalescence among the C_{60} within the host SWNT. The DWNT is the latest well-ordered all-carbon structure to be found [1], following fullerenes, multiwalled and single-walled carbon nanotubes (MWNT, SWNT) [2], nanohorns [3], and peapods [1,4]. Recently, Chen et al., [5] have reported charge transfer properties between bromine and DWNTs using resonant Raman scattering. They have found that the most of the charge resides on the outer wall of the DWNT confirming a molecular Faraday cage effect.

Experimental

The SWNTs used in this study were prepared using high temperature pulsed laser vaporization (PLV) of a graphite target containing Fe/Ni (0.6%-0.6% atomic) catalysts. The chemical purification of the PLV derived material was carried out by refluxing in 70% HNO_3 for 8 h at 160 ^{0}C. The suspension was neutralized by centrifugal decantation with distilled water and finally with ethanol. Then the purified SWNTs were dried and heated in dry air at 420 ^{0}C for 20 min. This last treatment was found to be necessary for opening the tube ends to allow the dopants to easily creep into the nanotubes. The doping of C_{60} into the inner hollow space of SWNTs was carried out in a sealed glass ampoule at 400 ^{0}C for 24 h by vapor phase reaction of C_{60} with SWNTs. The DWNTs were synthesized by annealing the peapods at 1200 ^{0}C in a vacuum better than 10^{-6} Torr. During the high temperature annealing in vacuum, the C_{60} molecules are found to coalesce between adjacent molecules within the host SWNT. The fully packed C_{60} molecules inside the SWNTs are completely transformed into a tubular structure forming DWNTs. Each sample was vacuum-degassed *in situ* in the TEP apparatus at 500 K before exposing to potassium. The doping-induced change of the thermopower, or Seebeck coefficient S, and the four probe resistance *R* were studied in a quartz reactor with; 20-mm inner diameter; ~25 cm in length equipped with a 2 3/4-in. knife-edge flange sealed via a Cu gasket to a standard multipin feedthrough flange. For *in situ* transport measurements, two chromel–Alumel thermocouples and two additional Cu leads were attached with small amounts of silver epoxy to four corners of the 4 mm× 4 mm sample to measure the TEP and the DC four-probe electrical resistance simultaneously. The sample holder with the sample attached to the electrical leads was loaded into the glass reactor together with a small, break-seal ampoule containing potassium. The reactor was evacuated to 10^{-7} Torr using a turbo molecular pump and degassed at 500 K while the time evolution of both R and S were recorded. Then the reactor was cooled down to room temperature and isolated through a high vacuum valve. The alkali metal was then released by shaking the reactor and breaking the break-seal on the alkali metal-containing ampoule. The surface of the alkali metal remained shiny throughout the experiment indicating the absence of any significant amount of oxygen or water in the reactor. The reactor was positioned in a temperature gradient in a horizontal furnace and heated to vaporize the alkali metal. The temperature gradient was chosen to provide efficient transport of alkali metal from the ampoule to the sample, avoiding excessive condensation of the unreacted potassium layer on the surface of the sample. At any time during or after the doping, we were able to stop the reaction by cooling the furnace and then measure the temperature dependence of R and S between 500 and 77 K by lowering the reactor into a dewar of liquid nitrogen. Further doping could then be carried out by repositioning the reactor in the furnace. Three independent experiments were carried out for SWNTs, peapods, and DWNTs all derived from the same initial material of SWNTs.

Results and Discussion

Figure 1 shows a typical *in situ* variation of the resistance R normalized to the resistance of pristine SWNT mat R_0 with exposure time to K vapor. An initial drop in *R* was observed when the alkali-metal temperature reached 400 K. Further sharp drops in *R* indicated with arrows in Fig. 1 were observed when the furnace temperature was stepped up by another 10 °C. We have increased the furnace temperature in steps in order to be able to observe the diffusion kinetics.

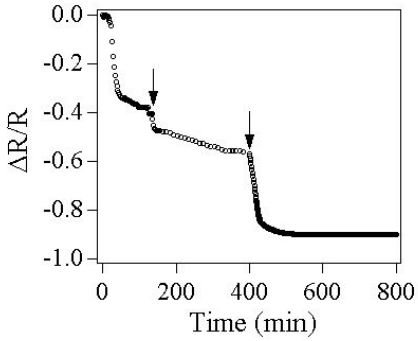

Figure 1. A typical *in situ* variation of four-probe dc resistance *R* of K-doped SWNT mats normalized to the *T*=400 K resistance of the pristine SWNT mat as a function of exposure time to K vapor.

The thermopower (S) of each air-exposed sample shows strong p-type behavior consistent with previous studies. Interestingly, in contrast to previous studies on SWNT materials, this p-type behavior of S remained essentially unchanged during degassing at 500 K in vacuum (<10^{-7} Torr). It has been shown previously [6] that the p-type behavior observed in air-exposed SWNTs can be easily driven n-type by in-situ degassing under these conditions. Further it has been shown that if the degassed SWNTs were exposed to oxygen at temperatures above 500 K, the thermopower is irreversibly changed to p-type, presumably due to strongly bound oxygen resulting in a C-O bond. It should be noted that the SWNTs used in this study are heated in dry air at 420 ^{0}C. For the peapod sample, the irreversible p-type behavior can be due to the same reason. Second possible explanation is that a small charge transfer between C_{60} and SWNTs can result in pinning the Fermi energy near the valance band edge independent of oxygen adsorption/desorption. Another possibility is that the the endohedral C_{60} blocks the oxygen molecules from desorbing out of peapods. The third scenario is more likely in explaining the irreversibility of p-type behavior in DWNTs. The annealing of peapod sample at 1200 ^{0}C in a vacuum <10^{-7} Torr

should be sufficient to remove all the oxygen adsorbed on the carbon surfaces. Any oxygen blocked by C_{60} could be trapped during the coalescence of the C_{60} molecules during the annealing.

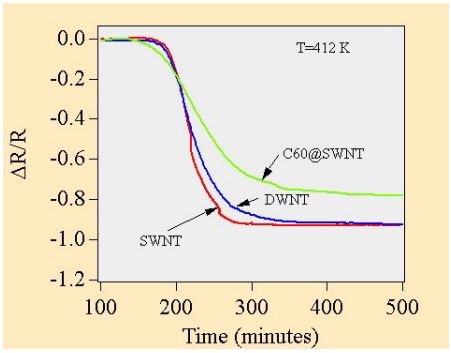

Figure 2. *In situ* variation of four-probe resistance *R* of K-doped SWNT, peapods, and DWNT mats normalized to the *T*=412 K resistance (before the doping started) as a function of exposure time to K vapor.

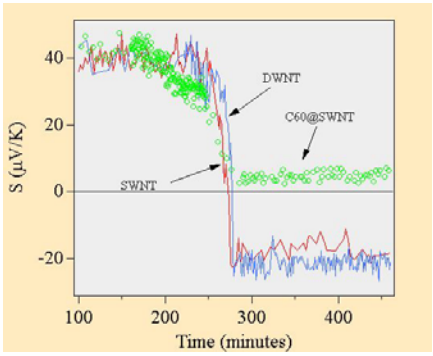

Figure 3. *In situ* variation of four-probe resistance *R* of K-doped SWNT, peapods, and DWNT mats normalized to the *T*=412 K resistance (before the doping started) as a function of exposure time to K vapor.

Fig .2 shows the K-doping effects of the resistance (normalized to the resistance of the undoped sample at T = 412 K) of the three samples, SWNT, peapods, and DWNT. They all show drastic drop of resistance of ~ 80-95 %. Interestingly SWNT and DWNT show almost the same change in resistance, while the change for peapod is somewhat less. Fig. 3 shows the concomitant results of the thermopower for the three samples during the K-doping. Again, SWNT and DWNT show very similar changes in TEP; starting ~ 40 μV/K, decreasing in magnitude, reversing the sign and eventually saturating ~ -20 μV/K. Most interestingly, the TEP of the peapod sample saturates only ~ 0 μV/K without reversing the sign.

Doping effects on both resistance and TEP suggest that the charge transfer properties between K and SWNT or DWNT are very similar consistent with the observations on charge transfer properties on Raman spectra of SWNTs and DWNTs. But peapods show entirely different behavior as can be expected due to the mediation of C_{60} during the charge transfer process. Raman studies on charge transfer in peapods have revealed competition between C_{60} and SWNTs during the charge transfer process. This behavior is not well understood and currently under theoretical investigation. A likely scenario is that the Fermi energy is pinned near the midpoint between the valence band and the conduction band due to the presence of C_{60}.

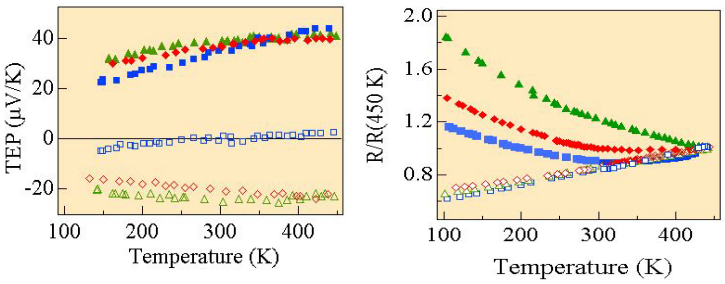

Figure 4 Temperature dependence of (a) Resistance R (b) TEP S before and after saturation doping with K for SWNTs, peapods, and DWNT mats.

Fig.4 shows the temperature dependence of the resistance and the TEP of the three samples before and after K-doping. Unfortunately, the low temperature data is for T > 100 K for obvious technical reasons. It is clearly seen that all three samples show typical temperature dependence of resistance and TEP characteristic of SWNTs before doping. After doping they show obvious metallic behavior.

Conclusions

In situ study of K-doping in SWNTs, C_{60}@SWNTs, and DWNTs has been done by monitoring resistance and thermopower. The data suggest that the charge transfer effects are similar in SWNTs and DWNTs, but drastically different in C_{60}@SWNTs. All three samples show p-type behavior before doping presumably due to oxygen doping. Degassing at 500 K under high vacuum is not sufficient to desorb oxygen suggesting stronger C-O bond.

References

(1) Bandow *et al.*, *Chem. Phys. Lett,* **2001**,. 337, 48
(2) Iijima S. and Ichihashi T., *Nature* (London), **1993**, 363, 603
(3) Iijima S. *et al.*, *Chem. Phys. Lett*. **1999**, 309, 165
(4) Smith B. W., Monthioux M., and Luzzi D. E., *Nature (London),* **1998**, **396**, 323
(5) Chen G. *et al*., Phys. Rev. Lett., **2003**, 90, 257403
(6) Sumanasekera *et al*., Phys. Rev. Lett., **2000**, 85, 1096